VIP *Very Important Paper*

Spatially Resolved Chiroptical Spectroscopies Emphasizing Recent Applications to Thin Films of Chiral Organic Dyes

Gianluigi Albano,[a] Andrea Taddeucci,[a, b] Gennaro Pescitelli,[a] and Lorenzo Di Bari*[a]

Chemistry–A European Journal
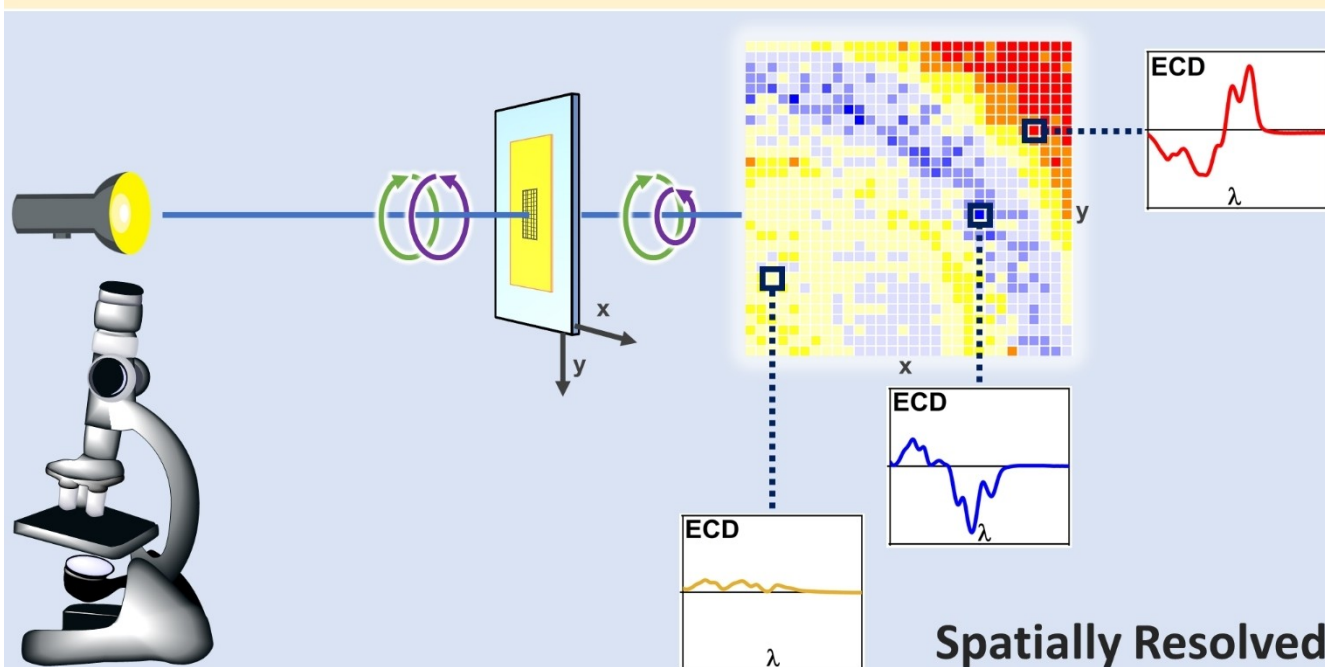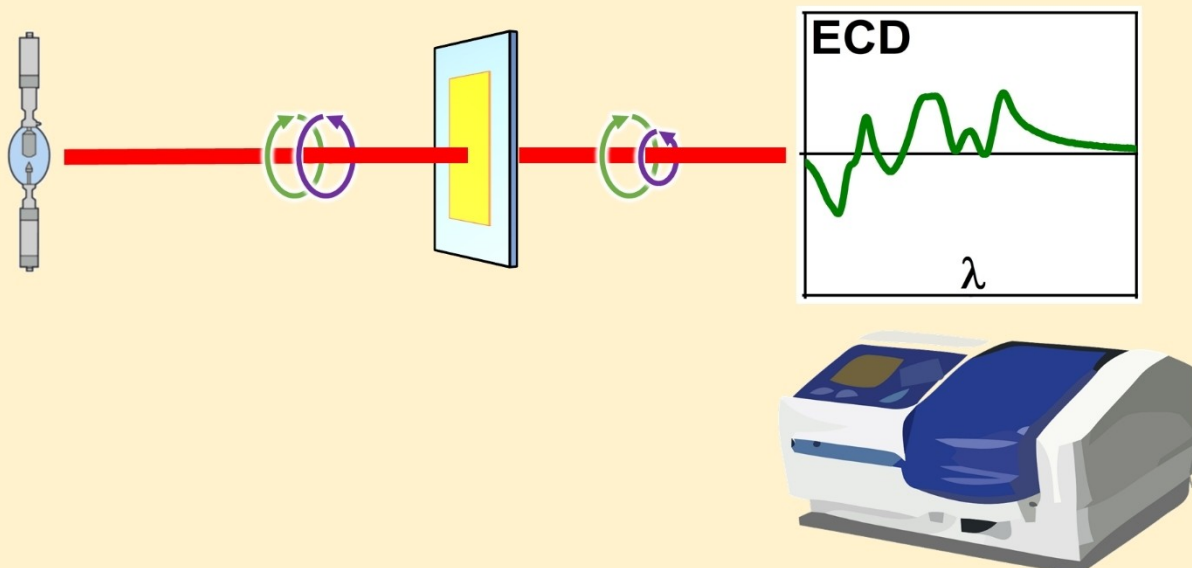
Review
doi.org/10.1002/chem.202301982

Chemistry Europe
European Chemical
Societies Publishing

Instrumental techniques able to identify and structurally characterize the aggregation states in thin films of chiral organic π-conjugated materials, from the first-order supramolecular arrangement up to the microscopic and mesoscopic scale, are very helpful for clarifying structure-property relationships. Chiroptical imaging is currently gaining a central role, for its ability of mapping local supramolecular structures in thin films. The present review gives an overview of electronic circular dichroism imaging (ECD*i*), circularly polarized luminescence imaging (CPL*i*), and vibrational circular dichroism imaging (VCD*i*), with a focus on their applications on thin films of chiral organic dyes as case studies.

1. Introduction

In the last twenty years, the general interest of organic and materials chemists in π-conjugated small molecules and polymers has greatly increased: thin films of these systems (typically showing thickness up to few hundred of nanometers) have found appealing applications as semiconducting active layers in devices for optoelectronics,[1] spintronics[2] and nanotechnology.[3] Compared to conventional inorganic semiconductors, organic π-conjugated materials feature easy processability and good mechanical properties, opening the way to the development of highly innovative flexible and printable devices.[4] The physico-chemical properties which are relevant to technological applications (that is, absorption and emission spectra, brightness, HOMO–LUMO energy gap, thermal stability, charge and exciton transport, magnetism etc.) are heavily modulated by the solid-state organization at different levels: one can envisage a hierarchy, from the first-order supramolecular arrangement,[5] i.e. on the low-nanoscale, up to microscopic and mesoscopic structures.[6] Several parameters may be adjusted to tweak the structural arrangement of π-conjugated systems in thin films. In the first place, one can think of acting on their chemical structure, for example modulating the conjugation length or the charge transfer character of electronic transitions through push-pull effects, introducing groups responsible for steric or other non-covalent interactions, and so on.[7] At the same time, the paramount effect of the deposition technique (drop casting, spin coating, spray coating, etc.) and post-deposition operations (in particular, solvent curing, thermal annealing and ageing) has been widely demonstrated.[8] This is due to the fact that in the thin film the same compound may give rise to polymorphism, that is, it can exist in varied ordered states. Each polymorph is characterized by different physico-chemical properties, such as charge transport, exciton lifetime, absorption or emission spectrum, magnetic properties.[6b,7c] Very often, owing to competing aggregation pathways active during thin-film fabrication or post-deposition operations, different polymorphs can coexist in the same film, segregated in local domains, while deposition and post-deposition techniques displace the equilibrium between the various forms.[9] This is responsible for apparently changeable emergent properties of the material, which may be hard to rationalize, without a precise knowledge of its intimate structure.

With this in mind, it is clear how important it is controlling the structural arrangement of the π-conjugated chains in thin films, through molecular design and by monitoring local order for optimizing the performance as semiconductive active layers.[6] Researchers have become increasingly aware of the importance of molecular chirality, through the introduction of enantiopure chiral moieties directly into the π-conjugated skeleton, or as side chains of the main π-conjugated backbone. The soft-matter nature of these thin films, which is so relevant to the above mentioned features of organic optoelectronic devices, means that perfect parallel and co-facial stacking between adjacent π-conjugated units is prevented. In this situation, neighbouring molecules must be tilted with respect to one another, which necessarily leads to chirality because the tilt can occur clock- or anticlockwise. While a disordered molecular aggregate is often undesirable in terms of properties,[10] chiral materials with controlled handedness can lead to well defined chiral stacks,[11] possibly reflected in large scale morphologies such twisted ribbons, helical fibers and other typical chiral nano/mesoscopic local textures.[12] Furthermore, a chiral supramolecular organization is highly desirable to ensure longer exciton lifetime[13] and avoid aggregation-induced fluorescence quenching.[14]

At the same time, the use of thin films of chiral organic dyes as semiconducting active layers in optoelectronic devices recently opened the way to a variety of innovative and unique technological applications: circularly polarized-organic field-effect transistors (CP-OFETs),[15] circularly polarized-organic light-emitting diodes (CP-OLED),[16] chemical[17] and electrochemical[18] sensors of chiral compounds, enantiopure chiral magnets,[19] electron spin filters,[20] as well as chiroptical switching in information technology.[21]

The solid-state arrangement of organic π-conjugated dyes is the result of competing weak non-covalent interactions and supramolecular chirality is generally dynamic and very sensitive to external stimuli and environment.[22] Therefore, instrumental techniques able to identify and structurally characterize the aggregated states in thin films of organic π-conjugated materials are very helpful for clarifying structure-property

[a] Dr. G. Albano, A. Taddeucci, Prof. G. Pescitelli, Prof. L. Di Bari
Dipartimento di Chimica e Chimica Industriale
Università di Pisa
Via Giuseppe Moruzzi 13, 56124 Pisa (Italy)
E-mail: lorenzo.dibari@unipi.it
Homepage: https://ricerca.dcci.unipi.it/cd-pisa.html

[b] A. Taddeucci
Diamond Light Source, Ltd.
Chilton, Didcot OX11 0DE (UK)

Chemistry–A European Journal | Review
doi.org/10.1002/chem.202301982

Chemistry
Europe
European Chemical
Societies Publishing

relationships, and therefore optimizing their performance as active layers for optoelectronic applications.[6] In particular, since self-assembly processes typically occur across multiple length scales, the use of distinct techniques is mandatory for a thorough characterization. Microscopy techniques such as atomic force microscopy (AFM), transmission electron microscopy (TEM) and scanning electron microscopy (SEM) are widely used for the characterization of thin films morphology on the 10–100 nm scale,[23] while conventional optical microscopy is typically applied for investigating samples at micrometric scale.[24] However, these techniques can hardly provide insight into the supramolecular organization at the first level of hierarchy, that is at the 1–10 nm scale. For chiral organic compounds, a crucial role in this context is played by chiroptical spectroscopies: electronic circular dichroism (ECD) provides very relevant information about the first level of supramolecular organization at the nanometer scale,[25] and it is employed to distinguish polymorphs, often very difficult to identify otherwise;[9] with luminescent systems, circularly polarized luminescence (CPL) provides information complementary to ECD.[26] Vibrational circular dichroism (VCD) provides an alternative picture because it is sensitive to chirality, like the former two techniques, but rather than focusing onto the π-conjugated moieties, it responds to normal modes, and for this reason to the overall skeleton.

It is worth emphasizing that the study of chiroptical properties in thin films is more complex than solutions, due to the potential interference of macroscopic anisotropies often present in the solid state, which may provide a significant contribution to the measured ECD and CPL spectra.[27] The experimental chiroptical signal, both in absorption (ECD) and emission (CPL), for a thin film is typically expressed as the sum of several contributions, two of which are the most relevant. On the one hand, an *intrinsic* component invariant upon thin film orientation with respect to the instrumental optical axis (that is, by rotation or flipping), reflecting the molecular and/or supramolecular chirality and thus referred to as *true CD*. On the other hand, a *non-reciprocal* component, also referred to as *apparent*, which is invariant upon sample rotation around the instrumental optical axis, but it inverts its sign by sample flipping: in other words, it consists in the inversion of the handedness of CP light component which is preferentially transmitted (in the case of ECD) or emitted (in the case of CPL) by the two opposite faces of the same film. Such non-reciprocal component arises from an interference interaction of macroscopic anisotropies present in the sample: between linear dichroism (LD) and linear birefringence (LB) in the case of non-reciprocal ECD contribution; between linear fluorescence anisotropy (f) and linear birefringence (LB) in the case of non-reciprocal CPL contribution.[28] Besides these *reciprocal* (*true*) and *non-reciprocal* (*apparent*) terms, which are *real* discriminations of left and right polarized radiation and are independent of the instrument used for their detection, artifacts can be present in the ECD and CPL spectra of thin films, due to the same macroscopic anisotropies (LD, LB, f) coupled with the non-ideal characteristics of spectropolarimeter optics and for this reason they provide different results on different instruments. All these terms can be identified and disentangled by
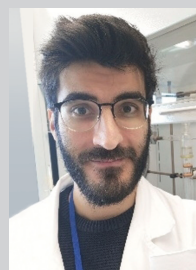
Gianluigi Albano received his M.Sc. (2015) and Ph.D. (2019) degrees in Chemistry cum laude from the University of Pisa. After three years as Post-Doc at the University of Bari Aldo Moro, from April 2023 he joined the University of Pisa as Junior Assistant Professor in Organic Chemistry. He is the recipient of the Flavio Bonati Prize 2022 of the Italian Chemical Society, as the best under 35 Italian researcher working in the field of Organometallic Chemistry. His activity is focused on different topics of Organic and Organometallic Chemistry, including the synthesis and chiroptical characterization of chiral π-conjugated dyes for innovative optoelectronic applications.

Andrea Taddeucci received his M.Sc. (2020) in Chemistry from the University of Pisa. From November 2020, he is joint Ph.D. student at Diamond Light Source and the University of Pisa, under the Marie-Sklodowska Curie Research and Innovation Programme. His research activity is focused on the synthesis and chiroptical characterization in thin film of chiral organic semiconductors. More recently, his activity focused mainly on the spatially resolved circular dichroism investigation of thin films, adopting highly collimated synchrotron radiation.

Gennaro Pescitelli received his M.Sc. and Ph.D. (2001) degrees in Chemistry from the University of Pisa and spent a postdoc period at Columbia University. He was appointed Associate Professor in Organic Chemistry at the University of Pisa in 2014. He is co-author of over 230 publications. His research is focused on spectroscopic and computational investigations of chiral organic molecules, especially natural products, metal compounds, organic crystals, organo-gelators, conjugated functional oligomers and polymers. He is associate editor of the journal Chirality (Wiley).

Lorenzo Di Bari received his M.Sc and PhD in Chemistry from the University and the Scuola Normale Superiore in Pisa. He became faculty Member at his Alma Mater in 1992. He is mainly interested in the experimental approaches for studying, characterizing and taking advantage of chirality of complex systems. He supervised many MSc and PhD theses and most of his former group members are now developing their independent academic careers worldwide.

Chemistry–A European Journal | Review
doi.org/10.1002/chem.202301982

Chemistry
Europe
European Chemical
Societies Publishing

Mueller Matrix polarimetry (MMP)[29] and Mueller Matrix spectroscopic ellipsometry (MMSE)[30] techniques.

Chiroptical spectroscopies such as ECD and CPL typically average light intensity measurement from beams with ~ 1 cm² cross sections. Such measurements are suited only to homogeneous isotropic samples. Thorough characterization of inhomogeneous and anisotropic samples requires spatial resolution, a possible solution being chiroptical imaging. Spatially resolved chiroptical spectroscopies (also named 2D-chiroptical spectroscopies) represent a useful tool for mapping and disentangling local supramolecular structures in thin films of chiral organic dyes: many different techniques able to perform electronic circular dichroism imaging (ECD*i*), circularly polarized luminescence imaging (CPL*i*), and even vibrational circular dichroism imaging (VCD*i*) measurements have been successfully developed, especially in the last years. In the present review we give an overview of all the aforementioned spatially-resolved techniques, emphasizing in particular their application for the study of thin films of chiral organic dyes. In the first part we shall discuss the strategies for ECD*i* measurements: after a historical excursus on the origin of ECD microscope, we shall critically examine the different approaches available for ECD*i* measurements of organic π-conjugated layers, emphasizing for each of them its strengths and weaknesses. In the final part of this section, we shall briefly discuss also the most relevant examples of spatially resolved Mueller matrix techniques. Then, we will move our attention onto the more recent (and less investigated) protocols for CPL*i* measurements of thin films of chiral organic dyes, including a few examples involving lanthanide complexes used as luminescent molecular probes of non-emitting chiral organic layers. Finally, we shall briefly overview the very recent studies on VCD*i* measurements.

All the experimental set-ups for spatially resolved chiroptical spectroscopies which will be presented below can be grouped into two different types of configurations. On the one hand, we shall consider the *localized chiroptical spectroscopy (LCS)* configuration, which can be achieved by focusing the light beam on a small point and by collecting the signal from that point only. This means that conventional schemes for chiroptical spectroscopy are coupled with sophisticated objectives and/or pinholes to cover an area typically of a few μm², in such a way one can measure the chiroptical spectrum of a specific point in the image. Systematic displacement of the sample on a XY (motorized) stage allows one to raster its surface and gain imaging. In this scheme, one may take full advantage of sensitive and accurate polarization optics and detection schemes of high quality spectropolarimeters, which can allow for measuring weak signals, somehow at the expense of spatial resolution. There are at least three different timescales to consider: switching between left- and right-handed light polarization, wavelength selection and XY scanning. There are several modes to combine them, according to the polarizing, the dispersion (to achieve wavelength selection) and the detection elements. Conversely, one may gain full images of the whole sample at once, typically through charge-coupled device (CCD) cameras or complementary metal-oxide semiconductor (CMOS) sensors, by introducing light polarizing elements

(typically, a linear polarizer coupled with a quarter wave plate or, alternatively, a photoelastic modulator) in the fundamental design of a microscope: this is the *circularly polarized microscopy (CPM)* configuration. In particular, the analysis of two different pictures of the same area taken with the right-handed and left-handed CP light (transmitted in the case of absorption, emitted in the case of luminescence) allows one to obtain the spatially resolved chiroptical maps at selected wavelengths. Understandably, CPM is a very simple technique for spatially resolved chiroptical measurements; at the same time, it may suffer from lesser sensitive and accurate polarization optics compared to the high quality spectropolarimeters used in the LCS configuration. In particular, since the maps are obtained by the difference of two different images, the CPM configuration has limited sensitivity and can be successfully applied only to samples characterized by large chiroptical signals (in terms of dissymmetry *g*-factor values) and spectra with broad bands.

2. Electronic Circular Dichroism Imaging (ECD*i*)

Despite the relatively recent interest over the last 15 years, ECD*i* measurements have an earliest origin: the idea of an ECD microscope was developed for the first time in 1982 by Maestre and Katz, who were interested in very localized ECD spectra of biological samples on a sub-cellular scale.[31] For this purpose, they developed their "micro-spectrophotometer" through the modification of a Cary 60 CD spectropolarimeter coupled with a standard Zeiss microscope: working in the wavelength range between 350 nm and 200 nm, the instrument was able to simultaneously measure the ECD and the UV absorption spectrum. The schematic representation of Maestre and Katz's ECD microscope instrumentation is depicted in Figure 1. The monochromatic light beam (generated by a suitable lamp equipped with a monochromator) was polarized horizontally with a linear polarizer (LP), then it was sent into a vertical direction by a front surface mirror and projected through the electro-optical modulator (EOM), responsible for the generation of the CP light. This latter was projected onto the microscope stage by means of a UV condensing system (that is, a Zeiss objective); the same type of lens was used to project the transmitted light beam, through a quartz relay lens, into the photomultiplier detector for signal recording and processing or toward a viewing port. The pinhole size was used to delimit the area of thin film sample to be measured. The analyzed surface area was typically in the range of few microns in diameter. To record the whole ECD spectrum and, simultaneously, the UV absorbance spectrum of the selected area, the mirror was moved to allow the photomultiplier to record the signal as a function of wavelength. The sampled area can be changed by moving the sample stage. Overall, this can be defined as a localized ECD measurement, while no systematic image is obtained. Therefore, this experimental set-up for ECD*i* measurements represents the first example of *LCS configuration*. The authors were well aware that their home-made ECD microscope was extremely sensitive to alignment parameters and optical artifacts such as linear birefringence. For this purpose, they
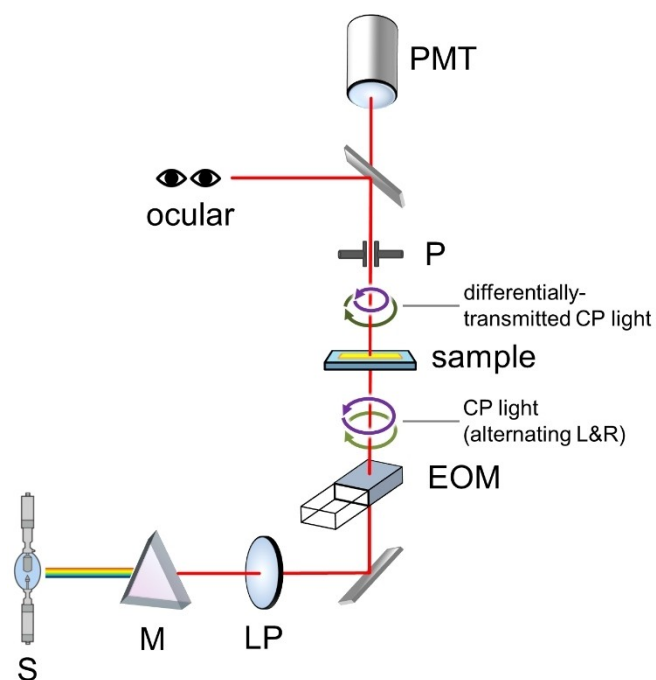
Chemistry–A European Journal

Review

doi.org/10.1002/chem.202301982

Chemistry Europe
European Chemical
Societies Publishing

Figure 1. Schematic representation of the home-built ECD microscope instrumentation developed in 1982 by Maestre and Katz. Legend: S, light source; M, monochromator; LP, linear polarizer filter; EOM, electro-optical modulator; P, pinhole; PMT, photomultiplier detector. Adapted with permission from Ref. [31]. Copyright 1982 John Wiley & Sons.

calibrated their instrumentation with standard samples of (+)-D-10-camphorsulfonic acid. The match between the spectra recorded with a benchtop ECD spectropolarimeter and with their home-built ECD microscope allowed them to exclude the occurrence of artifacts. Such instrumentation was used by Maestre and co-workers for the measurements of biological samples: human red blood cells and lymphocytes,[31] Chinese hamster tissues,[32] as well as dinoflagellate microalgae[33] and flesh fly *Sarcophaga bullata* samples.[34] These spatially resolved chiroptical measurements are important not only from a historical point of view, but also provided very important structural information on the above mentioned samples: in particular, they revealed the occurrence of chiral arrangements at the microscopic scale, such as dense superhelical structures of DNA molecules or chiral superstructures of chromatin which differentially scatter CP light, which could hardly be obtained by conventional ECD spectroscopy sampled on a wide area and would be totally lost with microscopy using unpolarized light.

Systematic errors and artifacts are inevitable in the field of polarization-modulation spectroscopy: on the one hand, measurements can be affected by instrumental defects, due to a misalignment in the optical set-up, window effects, imperfect optical and electronic components, and so on; on the other, macroscopic linear anisotropies often present in solid-state samples (linear dichroism and linear birefringence) can be responsible for spurious contributions in the ECD signals. Starting from these considerations, in 1990 Shindo et al. recognized that a greater variety of physical interactions can give rise to ECD signals:[35] the application of the Mueller matrix

approach[36] to their home-built ECD microscope revealed the occurrence of spurious contributions in their ECD*i* measurements. As it is well known, the crude ECD signals of solid state samples is typically the sum of various terms: i) an intrinsic contribution which is invariant upon sample orientation with respect to the instrumental optical axis (that is, rotation or flipping) reflecting the molecular and/or supramolecular chirality, named true CD; ii) a non-reciprocal contribution which is invariant upon sample rotation around the instrumental optical axis but it inverts its sign by sample flipping, named apparent CD or even LDLB, since it arises from an interference interaction between linear dichroism (LD) and linear birefringence (LB); iii) artifacts associated with the residual birefringence of the electro-optical modulator/photoelastic modulator, responsible of spurious signals when interacting with a sample exhibiting LD; iv) artifacts related to the residual linear polarization of the photomultiplier, interfering with the LB of the sample. Eventually, Shindo et al. concluded that the local ECD spectra recorded with Maestre and Katz's microscope on the microspots of thin film samples were actually not true circular dichroism signals, but only apparent circular dichroism due to LD and LB.

In the following fifteen years spatially resolved ECD measurements fell by the wayside, until in 2003 Kahr and co-workers built a new microscope for ECD*i*, based on a different approach:[37] in order to be independent of all the intrinsic technical limitations of the polarization-modulation instrument, they removed the electro-optical modulator and opted for a mechanical modulation of the CP light. As depicted in Figure 2, between the visible light source and the sample stage of a microscope they mounted a sliding interference filter, a rotating linear polarizer fixed to a gear driven by a stepper motor and a quarter wave plate. Right-handed and left-handed CP light at all wavelengths were produced by the alternating rotation of the linear polarizer to $+45°$ and $-45°$ with respect to the quarter wave plate easy axis, while continuously tuning the operating wavelength by the variable interference filter. The difference of the two signals, normalized by the regular absorption of the sample, yielded the ECD spectrum, which was finally corrected by difference with a reference area showing no CD. This comparatively slow polarization modulation technique allowed the authors to use a charge-coupled device (CCD) camera as detector, thus achieving true ECD images at selected wavelengths. This set-up represented the first example of instrumentation for spatially resolved chiroptical measurements through *CPM configuration*. This microscope was successfully used by Kahr et al. in the chiroptical investigation of organic and inorganic crystals: biaxial crystals of 1,8-dihydroxyanthraquinone showing intergrown enantiomorph domains,[37] lithium potassium sulphate crystals dyed during growth with Chicago sky blue or pyranine as a π-conjugated guests,[38] rhythmic phthalic acid precipitates showing heterochiral bisection.[39] Here, ECD*i* measurements were very helpful, revealing structural organizations which were undetected by X-ray diffraction and other techniques for crystal characterization. More recently, in the chiroptical investigation of polycrystalline D-sorbitol spherulites the authors have found persistent contributions due to
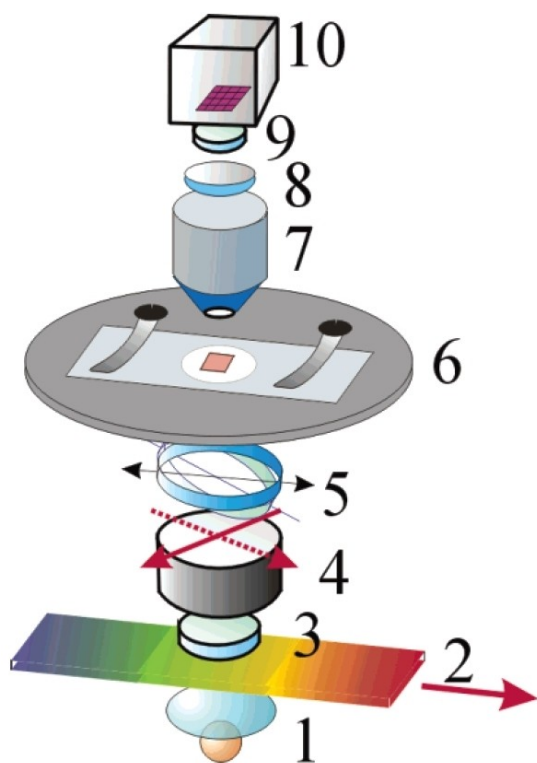
Chemistry–A European Journal

Review

doi.org/10.1002/chem.202301982

Chemistry Europe
European Chemical
Societies Publishing

Figure 2. Schematic representation of the visible light ECD microscope developed in 2003 by Kahr and co-workers. Legend: (1) light source; (2) sliding interference filter; (3) depolarizer; (4) rotating linear polarizer; (5) quarter wave plate; (6) sample mount; (7) objective; (8) projector lens; (9) depolarizer; (10) CCD-camera. Reproduced with permission from Ref. [37]. Copyright 2003 American Chemical Society.

sample heterogeneity encountered along the light propagation direction.[40]

Following these pioneering early works, the first spatially-resolved chiroptical study on thin films of organic π-conjugated materials was described only in 2008 by Watarai et al.:[41] drop-casted samples of cationic 5,10,15,20-tetrakis(*N*-methylpyridinium-4-yl)-21*H*,23*H*-porphine (TMPyP)/DNA complex were investigated by ECD*i* measurements thanks to the development of a simple home-built ECD microscope, obtained by combining a couple of objective lenses with a CCD camera installed in the sample chamber of a benchtop spectropolarimeter. In particular, they were able to measure both the macroscopic ECD spectrum (9×9 mm area) in the absence of any objective lens, and the local ECD spectra (60×60 μm area) by using the objective lenses; at the same time, a beam splitter and a mirror were introduced into the beam path to observe and snap sample images with the CCD camera. ECD*i* investigation of the TMPyP/DNA thin film revealed local domains with different structural arrangements: on the one hand, micro-spots with local ECD spectra showing a well-defined CD couplet between 400 nm and 450 nm, due to the exciton coupling of TMPyP molecules externally bound to DNA; on the other hand, micro-spots with local ECD spectra characterized by a single positive band in the same wavelength range, suggesting a groove binding mode of interaction between TMTyP and DNA.

Interestingly, the macroscopic ECD spectrum of the whole sample revealed very weak signals: this was due to an averaging effect of the two different types of local domains with different local ECD profiles, thus demonstrating for the first time the power of spatially resolved chiroptical spectroscopies in the elucidation of concurrent aggregation modes.

In 2012, Finazzi and co-workers developed an interesting new set-up for ECD*i* investigations, falling into the *CPM configuration*, based on two-photon fluorescence (TPF) scanning confocal microscopy (Figure 3a).[42] A pulsed laser beam (pulse duration ~400 fs), acting as the illumination source of the microscope, passed through an optical fiber, then it was collimated and further filtered from spurious fluorescence. The resulting linearly polarized light was transformed into circularly polarized using a quarter wave plate or, alternatively, a photoelastic modulator, and then sent to the sample through a strain-free microscope objective. The radiation collected by a second strain-free objective was filtered by a short-pass filter to block the excitation wavelength, and finally sent to a photomultiplier. The instrumentation worked in two different operation modes, static and dynamic. In the static imaging mode, a quarter wave plate was used to illuminate the thin film sample with left- and right-handed CP light, and two subsequent images (one for each CP state of light) were recorded sequentially by the photomultiplier in counting mode. In the dynamic imaging mode, a photoelastic modulator (PEM) modulated the excitation beam between left-handed and right-handed CP light at 50 kHz frequency, and a ECD*i* map was recorded using the photomultiplier in current mode and lock-in signal demodulation. In this work, the two-photon fluorescence scanning confocal microscopy was applied to the ECD*i* study of thermally annealed spin-coated samples of poly[9,9-bis((3*S*)-3,7-dimethyloctyl)-2,7-fluorene]. Such polymer exhibited intriguing chiroptical features: Meskers et al. found only a weak positive ECD band ($g_{abs} = +3.0 \cdot 10^{-4}$ at 400 nm) for freshly-prepared spin-coated samples, attributable to a substantially true circular
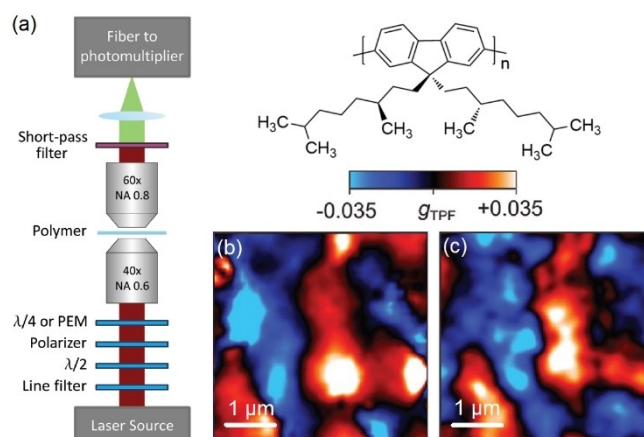
Figure 3. (a) Schematic representation of the two-photon fluorescence (TPF) scanning confocal microscopy for ECD*i* developed in 2012 by Finazzi and co-workers. ECD*i* investigation of thermally annealed thin films of poly[9,9-bis((3*S*)-3,7-dimethyloctyl)-2,7-fluorene]: 2D maps of the dissymmetry factor values g_{TPF} collected in (b) dynamic mode and (c) static mode. Adapted with permission from Ref. [42]. Copyright 2012 American Chemical Society.

Chemistry–A European Journal

Review
doi.org/10.1002/chem.202301982

Chemistry
Europe
European Chemical
Societies Publishing

dichroism arising from the supramolecular helical arrangement of individual π-conjugated chains.[43] Surprisingly, Neher et al. observed a strong negative ECD band ($g_{abs} = -0.15$ at 403 nm) after a prolonged thermal annealing in the liquid crystalline state, attributable to a non-reciprocal circular dichroism contribution due to the rearrangement into helically overlapped layers of aligned polymer chains.[44] For thermally annealed films of this polymer, the 2D maps of the dissymmetry factor g_{abs} recorded in dynamic mode (Figure 3b) and static mode (Figure 3c) revealed neighbouring areas (few micrometres of diameter) with opposite g_{abs} signs, represented by the blue and red zones, suggesting the existence of local domains with two different structural chiral configurations: one could be considered responsible for the large non-reciprocal contribution of the global ECD spectrum, while the other could give rise to the weaker true-CD term.

Narushima and Okamoto's research group dedicated several efforts to the development of instrumental set-up for ECD*i* investigations. In 2013, they reported a polarization modulated-scanning near-field optical microscopy (PM-SNOM) imaging system, falling into the *LCS configuration*, based on a collection-mode aperture-type scanning near-field optical microscope (SNOM) combined with a conventional ECD spectropolarimeter (Figure 4).[45] Emitted by a suitable lamp, the light beam passed through a linear polarized and a photo-elastic modulator, then was focused on the sample through an objective lens; the transmitted light was collected through the aperture of an optical-fiber probe and sent to a photomultiplier tube; finally, the intensity was converted to the local ECD signal through lock-in detection. Images were obtained thanks to a motorized XY-translational stage. Although this PM-SNOM instrumentation was first applied for the nano-imaging of 2D chiral metal nanostructures (S-shaped gold nanostructures) on glass substrates fabricated via electron-beam lithography,[45–46] more recently it was adopted by Monsù Scolaro, Patanè et al. for the ECD*i* study of single ribbon-like nanosized *J*-aggregates formed by acid-induced aggregation of tris-(4-sulfonatophenyl)phenylporphyrin (TPPS$_3$).[47] Interestingly, ECD*i* maps upon near-field excitation at 473 nm revealed that the molecules forming the nanoribbon have an inherently chiral structure at the local scale.

In the PM-SNOM technique, the polarization-modulation method was made possible by means of a PEM: despite its
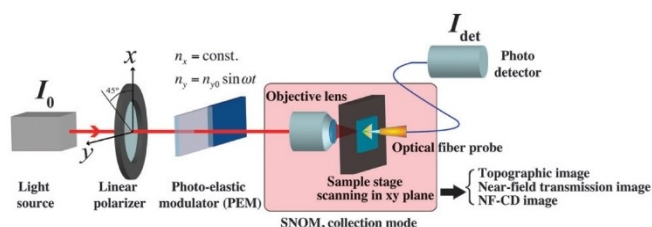
invaluable advantages, it could be responsible for spurious contributions and artifacts in the ECD maps, due to intrinsic technical limitations (e.g., non-linear response of optical elements, residual strain in the light modulation, and so on). In order to overcome these issues, in 2016 Narushima and Okamoto's group proposed the development of a new, PEM-free set-up for ECD microscopy, via discretely modulated circular polarization (Figure 5).[48] In this new system, once again belonging to the *LCS configuration*, the light beam emitted from the source passed through a linear polarizer filter, and the resulting linearly polarized light reached a polarization beam displacer of calcite crystal, which produced two spatially separated parallel beams with mutually orthogonal linear polarization. The horizontally and vertically polarized beams were sent to a rotary mechanical chopper, which let them to pass alternately without temporal overlap. Passing through a second beam displacer, the two chopped linearly polarized beams were recombined in a single beam with the same optical axis; finally, a quarter wave plate converted the coaxially combined horizontally and vertically polarized beams into, respectively, left-handed and right-handed CP light, which was directed to the sample. The transmitted CP light was focused through an objective lens onto the pinhole, then it was detected by a single-channel photomultiplier tube detector to give a local ECD signal, corresponding to a diameter of approximately 2.5 μm on the sample plane; the final 2D maps could be obtained by scanning local ECD signals on the sample surface. As for the previous PM-SNOM system, in this case too Narushima and Okamoto's group applied their new set-up for the ECD*i* investigation of two-dimensional arrays of chiral (swirl shape) gold nanostructures.[48] However, more recently, its use was successfully extended to crystalline particles of a microporous chiral metal–organic framework,[49] thin films of chiral plasmonic materials (gold nanoparticles incorporated within chiral liquid crystal matrices)[50] and crystals of the chiral superconductor κ-NCS.[51] Although the discretely modulated
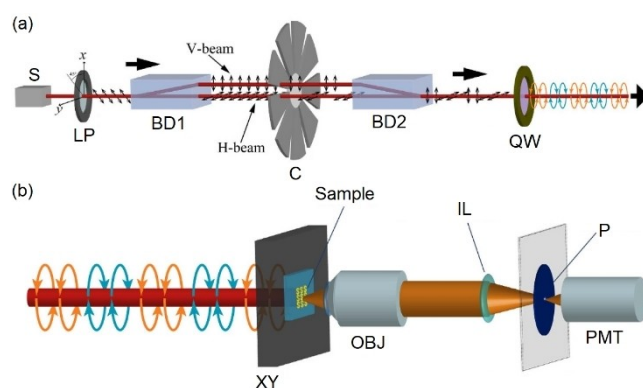

Figure 5. Schematic representation of the discretely modulated circular polarized light ECD microscope developed in 2016 by Narushima and Okamoto: (a) preparation of the modulated CPL beams; (b) transmission-mode ECD microscope with sample scanning. Legend: S, light source; LP, linear polarizer; BD1, first polarization beam displacer; C, rotatory mechanical chopper; BD2, second polarization beam displacer; QW, quarter wave plate; XY, closed-loop XY stage; OBJ, objective; IL, imaging lens; P, pinhole; PMT, photomultiplier tube detector. Adapted from Ref. [48] under Creative Commons Attribution 4.0 International License, 2016 Springer Nature.

Figure 4. Schematic representation of the polarization modulated-scanning near-field optical microscopy (PM-SNOM) imaging system developed in 2013 by Narushima and Okamoto. Reproduced with permission from Ref. [45]. Copyright 2013 the PCCP Owner Societies.

Chemistry–A European Journal

Review

doi.org/10.1002/chem.202301982

Chemistry Europe
European Chemical
Societies Publishing

circular polarized light ECD microscope was not used for the investigation of local supramolecular structures in thin films of purely organic materials, the obtained ECD*i* maps were reasonably free from spurious contributions due to the interaction of macroscopic anisotropies of samples with the non-ideal characteristics of spectropolarimeter optics: the authors thoroughly evaluated the residual anisotropy of both the optics and the detector, concluding that such kind of artifacts amounted to variations of the dissymmetry factor values g_{TPF} smaller than ± 0.003.

A system for micro-spot ECD*i* measurements through the *LCS configuration* was described in 2016 by Percec and co-workers, based on a pinhole masked sample cell put in the beam path of a benchtop ECD spectropolarimeter and settled on an XY translation stage.[52] This home-built set-up was equipped with a pair of reflective objective lenses between the ECD spectropolarimeter and the pinhole mask, in order to reduce undesirable optical aberration and give a wider range of measurement from the near-UV to visible wavelengths. Such micro-spot ECD*i* measurements were performed on thin films of racemic perylene bisimide (PDI) bearing 3,7-dimethyl-1-octyl chains (Figure 6a): while the ECD spectrum of the whole sample showed negligible signals, micro-spot ECD*i* maps revealed the existence of local domains containing chiral columnar supramolecular architectures of a single handedness, responsible for strong ECD signals (Figure 6b–c). The authors concluded that deracemization took place between left- and right-handed homochiral supramolecular columns in the crystal state (Figure 6d).[52–53] It is worth emphasizing that such chiral PDI was ideal to be investigated by ECD*i*: it exhibited a cooperative nucleation mechanism for helical supramolecular polymerization and the occurrence of multiple aggregation pathways. Similar micro-spot ECD*i* experiments were then applied by Choi and co-workers to study local helical microdomains of an achiral
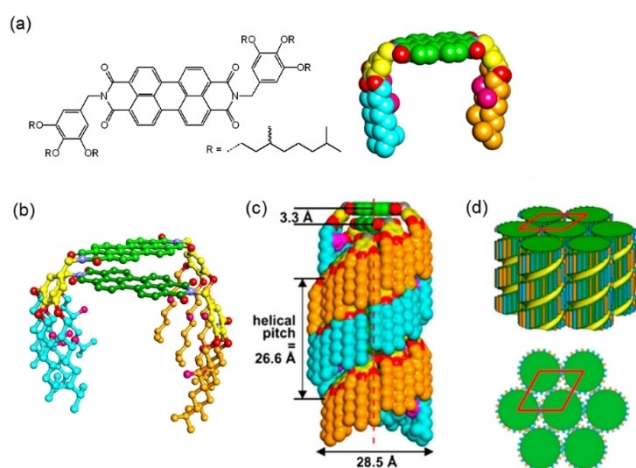
nematic liquid crystal refilled into chiral nanoporous thin films of a reticulated polyacrylate.[54] This was made possible by the small beam diameter ($< 10 \ \mu m$), obtained by using focal-reducing optics between the benchtop ECD spectropolarimeter and the pinhole mask, which was smaller than the dimension of local domains.

A system for ECD*i* investigation based on the *CPM configuration* was recently patented by Hamamatsu Photonics,[55] consisting of a Xe lamp as light source, monochromatic filter, linear polarizer, photo-elastic modulator, sample holder (7.7×7.7 mm window) and CCD camera. This instrumentation was applied in 2016 by the Yamaguchi's group for the study of a self-catalytic phenomenon of a 1:1 mixture of pseudoenantiomeric aminomethylene-helicene oligomers, (*P*)-tetramer and (*M*)-pentamer, in the formation of hetero-double helices from random coils (Figure 7).[56] More in detail, they found that hetero-double helices **B** and **C** were formed when a solution of random coil **A** in fluorobenzene was cooled: cooling **A** provided **B**, which was slowly converted to **C** (Figure 7a). Moreover, kinetic studies revealed the involvement of a self-catalytic reaction in the formation of hetero-double helices **B**; that is, **B** catalyzed the conversion of random coils **A** to form **B** itself. Although ECD*i* measurements were carried out only on solution samples, they were very helpful in providing information on the homogeneous-heterogeneous transition under cooling conditions: as depicted in Figure 7b, the tip of meteor-like dark domains with negative ECD at 320 nm appeared, which was consistent with the formation of hetero-double helix **B**, characterized by a negative signal at 320 nm in the ECD spectrum recorded with a conventional spectropolarimeter.
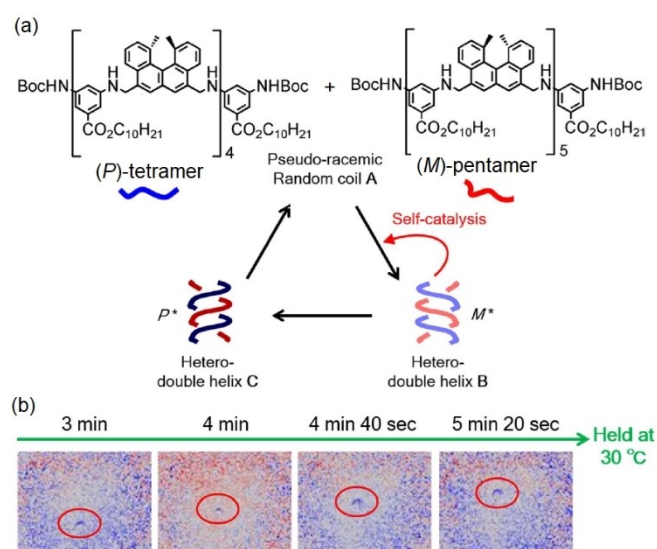

Figure 6. Self-assembly of chiral PDI investigated with micro-spots ECD*i* measurements by Percec and co-workers. Single molecules of chiral PDI (a) self-assembled into twisted dimers (b), held together by π-stacking interactions, which then aggregated to form helical supramolecular columns (c). The columns with same handedness packed into a hexagonal pattern retrieved in the crystal structure (d). Adapted with permission from Ref. [53]. Copyright 2020 American Chemical Society.

Figure 7. (a) General scheme of formation of hetero-double helices **B** and **C** from a 1:1 mixture of of pseudoenantiomeric aminomethylenehelicene oligomers, (*P*)-tetramer and (*M*)-pentamer, in the random coil state **A**. (b) ECD*i* maps recorded at 320 nm for a 1:1 mixture of (*P*)-tetramer and (*M*)-pentamer in fluorobenzene (total concentration 5.0×10^{-4} M) during a cooling experiment from 70 to 30 °C and then held at 30 °C for 20 min. The blue spots indicated by a red oval correspond to meteor-like dark domains with negative ECD. Adapted with permission from Ref. [56]. Copyright 2016 John Wiley & Sons.

Chemistry–A European Journal

Review
doi.org/10.1002/chem.202301982

Chemistry Europe
European Chemical
Societies Publishing

A further custom-built set-up for ECDi measurements was developed in 2019 by Hud et al., where a Jasco 810 ECD spectropolarimeter was equipped with a cuvette scanner (mapping a pattern of thirteen 24-mm long parallel traces separated by 0.5 mm) and the incident light beam was restricted to a circular cross section having 0.8 mm diameter.[57] This system, which is one of the most classic examples of LCS configuration, was successfully applied to study supramolecular polymers of achiral nucleobase mimics: the authors discovered a spontaneous symmetry breaking in the aggregation of 2,4,6-triaminopyrimidine with a cyanuric acid bearing a hexanoic acid tail, which organized into hydrogels exhibiting ECD signals (although with intensity and sign randomly distributed for different batches, since the symmetry breaking may occur stochastically in both directions). The ECDi maps of these hydrogels, in the form of thin films (0.01 mm of thickness) confined between two quartz plates, revealed a patchwork of macroscopic domains with ECD spectra varying in both intensity and sign, which suggested the existence of different domains composed of chiral superhelical structures with opposite handedness (Figure 8).

In 2022, Lenzer and co-workers developed a new instrumentation for both ECDi and CPLi measurements, attributable to the CPM configuration, based on a wide-field microscopy able to achieve a spatial resolution of ~500 nm.[58] The set-up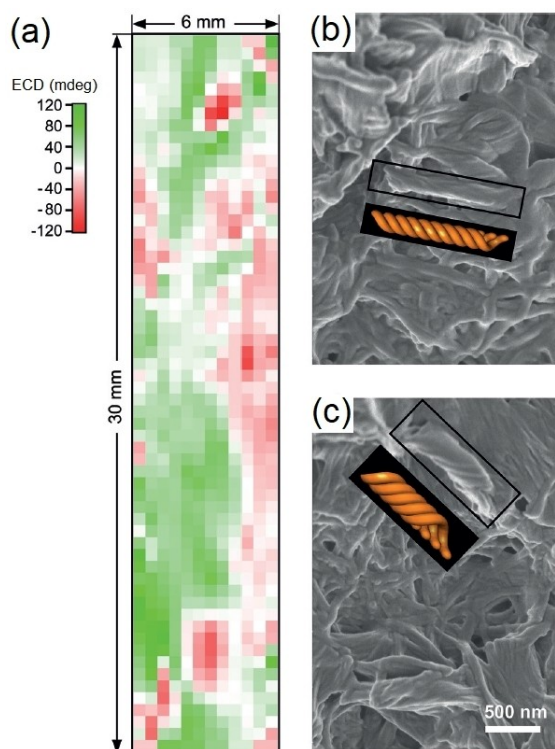 for ECD microscopy involved a halogen lamp as light source, coupled with a linear polarizer and a broadband quarter wave plate, which illuminated thin film samples with CP light. The transmitted light was collected by a microscope objective and sent through a bandpass filter to a non-polarising 50:50 beam splitter: one part of the beam was detected by a CCD camera (able to obtain ECDi map images), the other was focused by a quartz lens into an optical quartz fiber connected to a spectrograph equipped with a CCD detector (to record local ECD spectra). In particular, both the spatially resolved ECD maps at selected wavelengths and the ECD spectra of local spots were obtained from two different measurements, where the easy axis of the quarter wave plate was set at either $+45°$ or $-45°$ with respect to the linear polariser axis. In their first work, Lenzer and co-workers applied this ECD microscopy set-up for the investigation of supramolecular chirality in spin-coated thin films of chiral poly((9,9-bis[(3S)-3,7-dimethyloctyl]fluorenyl-2,7-diyl)-alt-(benzo[2,1,3]thiadiazol-4,8-diyl)), shortly known as c-PFBT.[58] The ECD and g_{abs} images at 470 nm recorded for a $80\times60\ \mu m^2$ area of the thin film with a 500 nm spatial resolution (Figures 9a–b) showed island-like structures with a granular appearance, in agreement with the optical microscopy images under cross-polarized filters obtained for a c-PFBT film in a previous study of Meijer et al.,[59] indicating a disordered multi-domain liquid-crystalline arrangement. The g_{abs} values collected in the 2D map were processed into a histogram (Figure 9c), well described by a Gaussian distribution, with $g_{abs}^{max} = -0.29 \pm 0.05$. The authors excluded the occurrence of non-reciprocal contributions in the ECD signals, as well as of other artifacts due to macroscopic anisotropies, by checking the invariance of ECDi images upon sample rotation and flipping.

The same ECD microscopy system was used very recently in the study of the chiral induction exerted by two helicene-type additives, that is, 2,2′-dimethoxy-5,5′,6,6′-tetrahydro-1,1′-bidibenzo[c,h]acridine **A** and its methylene-bridged analogue **B**, in thin films of achiral poly-[(9,9-di-n-octylfluorenyl-2,7-diyl)-alt-(benzo[2,1,3]thiadiazol-4,8-diyl)] (F8BT) co-polymer.[60] ECD images at 470 nm of spin-coated samples of F8BT blended with both enantiomers of the unbridged helicene-type compound **A** (Figure 10a–b) showed a strong chiral induction of opposite

Figure 8. (a) ECDi map of hydrogels of 2,4,6-triaminopyrimidine with a cyanuric acid bearing a hexanoic acid tail as thin films (0.01 mm of thickness) confined between two quartz plates. (b, c) SEM images showing helical bundles of the same hydrogel at two different imaging locations. Orange structures are idealized interpretations of the helical bundles boxed in panels (b) and (c). Reproduced with permission from Ref. [57]. Copyright 2019 John Wiley & Sons.

Figure 9. (a) ECD microscopy image and (b) g_{abs} microscopy image at 470 nm of spin-coated thin films of chiral co-polymer c-PFBT, recorded for a $80\times60\ \mu m^2$ area with 500 nm spatial resolution (scale bar: 25 μm). (c) Distribution of the g_{abs} values collected in the panel b for the $80\times60\ \mu m^2$ area of the sample. Reproduced from Ref. [58] under Creative Commons Attribution 4.0 International License, 2022 Springer Nature.
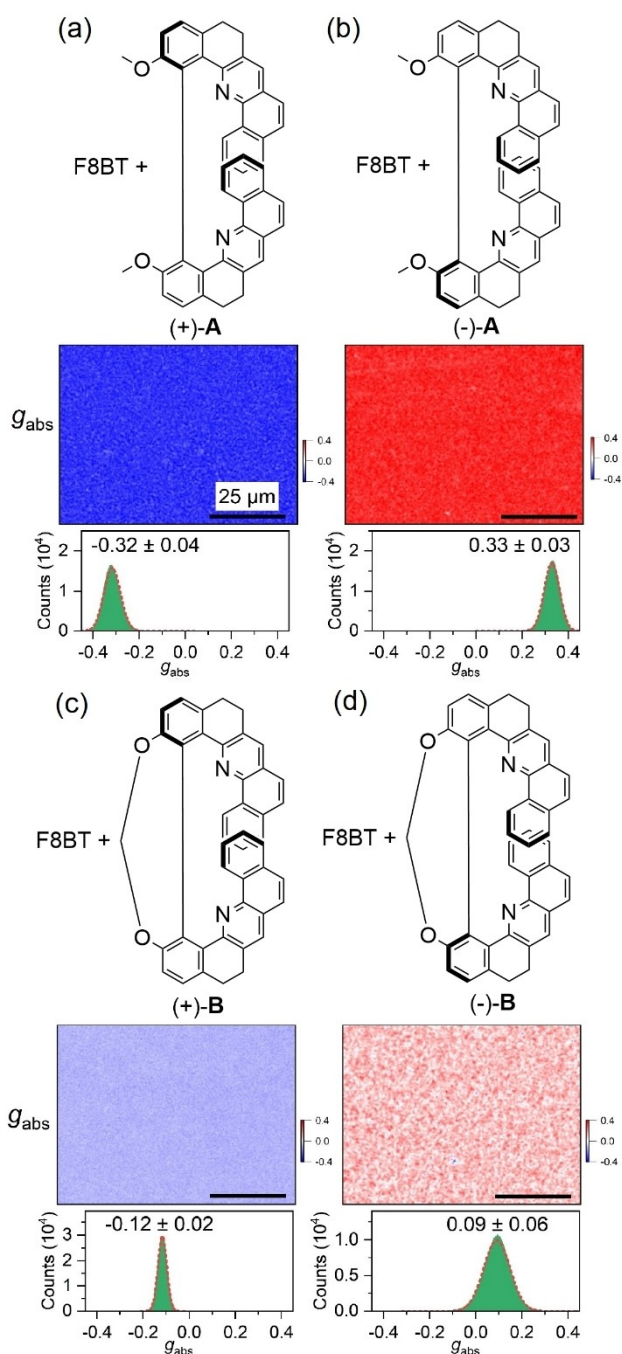
Chemistry–A European Journal

Review

doi.org/10.1002/chem.202301982

Chemistry
Europe
European Chemical
Societies Publishing

Figure 10. Absorbance dissymmetry factor g_{abs} microscopy images at 470 nm, recorded for a 80×60 μm^2 area with 500 nm spatial resolution (scale bar: 25 μm), and corresponding distributions measured for spin-coated thin films of achiral co-polymer F8BT blended with helicene-type additives: (a) F8BT/(+)-**A**; (b) F8BT/(−)-**A**; (c) F8BT/(+)-**B**; (d) F8BT/(−)-**B**. Adapted from Ref. [60] under Creative Commons Attribution 4.0 International License, 2022 John Wiley & Sons.

sign (maximum $g_{abs}=-0.32$ for F8BT/(+)-**A** and +0.33 for F8BT/(−)-**A**); the images exhibited island-like granular structures of micrometer dimensions, consistent with a statistical orientation of the individual copolymer domains. Interestingly, such a texture was similar to that observed in a previous work for thin films of the intrinsically chiral polyfluorene copolymer c-PFBT.[58]

The chiral induction of the methylene-bridged helicene-type compound **B** on the achiral F8BT led to qualitatively similar results: ECD maps (Figure 10c–d) revealed the same type of island-like granular structures, even if the chiral induction was weaker, as shown by the pale blue and red colors (maximum $g_{abs}=-0.12$ for F8BT/(+)-**B** and +0.09 for F8BT/(−)-**B**). It is worth emphasizing that thermal annealing of all these blends was mandatory to obtain a strong chiral response, while all pristine blends were ECD-silent. Moreover, no changes in the chiroptical response of 2D maps was observed upon sample rotation and flipping. This fact excluded the occurrence of non-reciprocal contributions and of spurious signals due to linear anisotropies; the g_{abs} values recorded in the ECD microscopy images were due to true circular dichroism.

An innovative approach for the ECDi investigation of thin films of organic dyes was developed in the last years by Siligardi and Di Bari's research groups, based on the highly collimated synchrotron radiation (SR) of Diamond Light Source B23 beamline.[61] The synchrotron radiation electronic circular dichroism imaging (SR-ECDi) technique is based on the collection of local ECD spectra for each pixel of a selected grid array area, mapped with a motorized XY stage having spatial resolution down to ~0.05×0.05 mm^2; these local ECD spectra can be processed into maps showing the ECD intensity (or other quantities, see below) at a selected wavelength vs. x-y coordinate (Figure 11). Although the final results might appear similar to other ECDi microscopy techniques based on the *LCS configuration*, SR-ECDi takes full advantage of the complete circular polarization of SR light attaining the lowest limit of quantitation with maximum accuracy of ECD signals.[62]
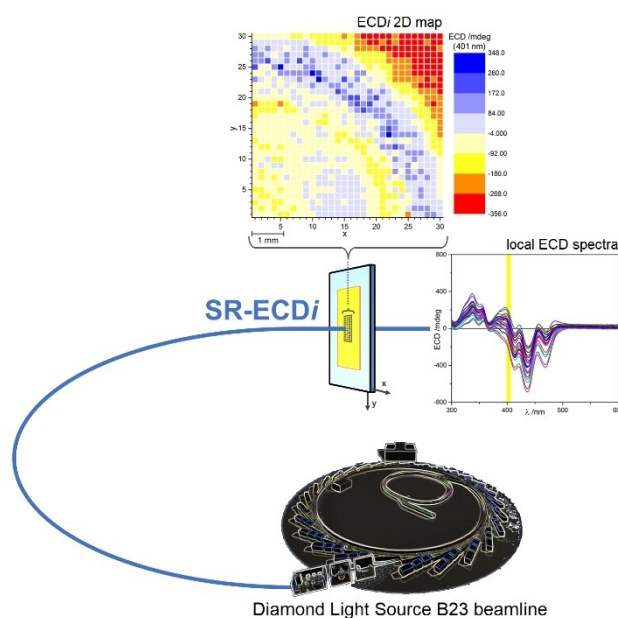
Figure 11. General scheme of the SR-ECDi technique developed by Siligardi and Di Bari's research groups for the investigation of thin films of chiral organic dyes: the highly collimated synchrotron radiation of Diamond Light Source B23 beamline produced local ECD spectra for each pixel of a selected grid array area, with spatial resolution down to ~0.05×0.05 mm^2; these local ECD spectra could then be processed into 2D map images.

Chemistry–A European Journal

Review
doi.org/10.1002/chem.202301982

**Chemistry
Europe**
European Chemical
Societies Publishing

SR-ECD*i* was applied for the first time in 2017 to study thin films of a poly(*p*-phenyleneethynylene) functionalized with chiral D-leucine groups (indicated as D-Leu-PPE), demonstrating the impact of deposition technique (spin coating vs. drop casting) and post-deposition operations (pristine samples vs. solvent annealed samples) on the chiroptical properties.[63] For each thin film, 25 ECD spectra were measured scanning a 5×5 grid array area with 1 mm step size and a beam diameter of 1 mm, revealing that apparently homogeneous films were actually characterized by local polymorphism. Spin-coated samples of D-Leu-PPE displayed a negligible ECD spectrum with the benchtop spectropolarimeter immediately after deposition (Figure 12a), meaning they could be considered as a frozen representation of the molecular arrangement in solution (that

is, the polymer did not have the necessary time to reach a stable supramolecular organization). However, SR-ECD*i* investigation (Figure 12b) revealed different ECD features for each spot of the investigated area of the as-cast film: this indicated that some chiral proto-aggregation occurred in different domains of the as-cast film. When the same samples were subjected to a short (few minutes) solvent annealing, the global ECD spectrum recorded on the whole sample drastically changed, with the formation of a structured positive band between 400 and 500 nm (Figure 12c). The corresponding SR-ECD*i* (Figure 12d) revealed a variety of different local ECD spectra: some of them showed a weak positive band, while other exhibited a sign inversion between 450 and 500 nm (similar to the global ECD spectrum of D-Leu-PPE after
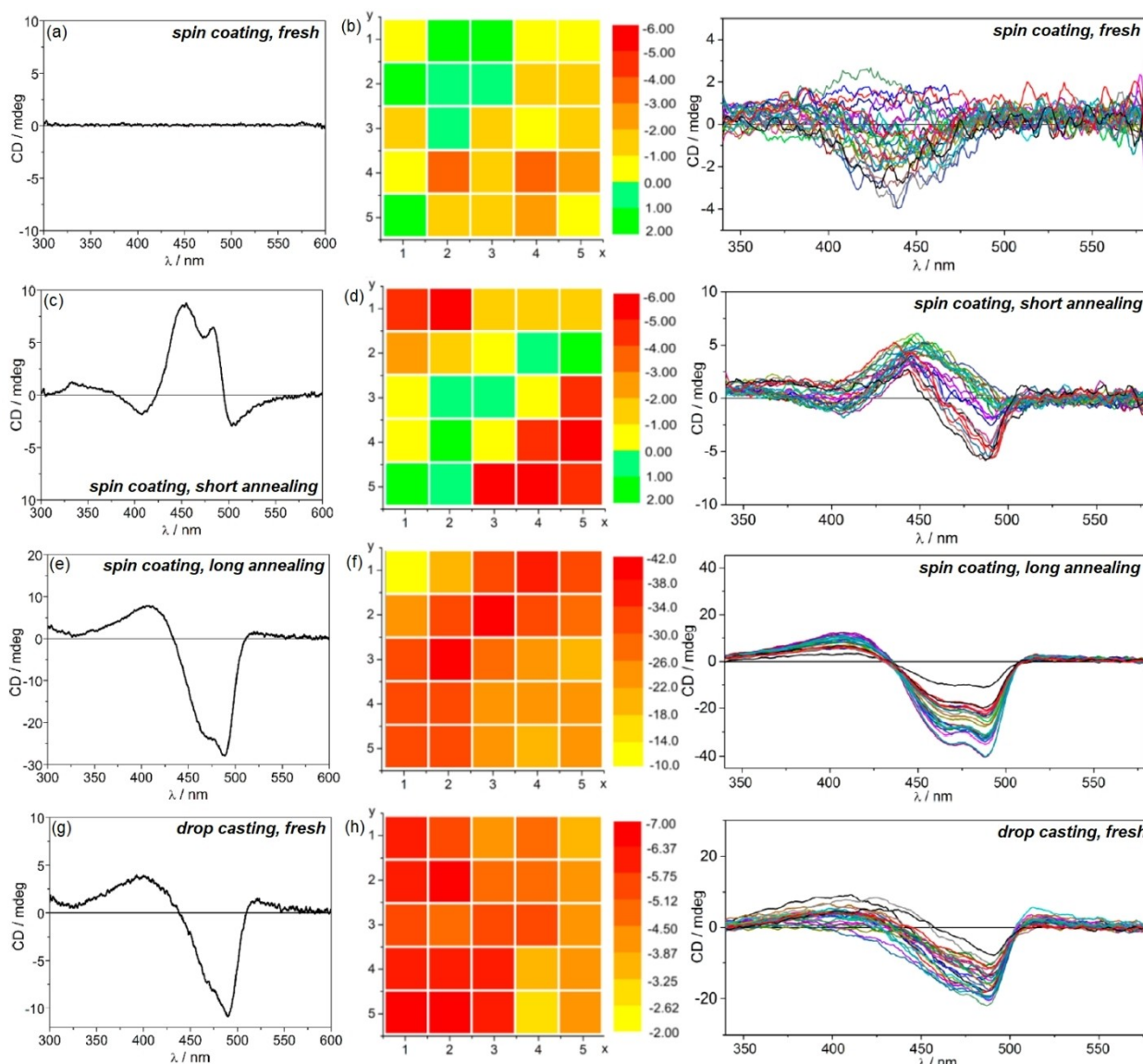

Figure 12. Left column: ECD spectra of thin films of chiral D-Leu-PPE recorded with a benchtop spectropolarimeter for (a) spin-coated sample, freshly prepared; (c) spin-coated sample, after short solvent annealing; (e) spin-coated sample, after long solvent annealing; (g) drop-casted sample, freshly prepared. Middle and right columns: SR-ECD*i* investigation of thin films of chiral D-Leu-PPE, performed by mapping a 5×5 grid array area with 1 mm step size and a beam diameter of 1 mm: local ECD spectra recorded for the 25 spots and 2D colour maps of ECD intensity at 436 or 490 nm vs. x-y (red/yellow/green hues) recorded for (b) spin-coated sample, freshly prepared; (d) spin-coated sample, after short solvent annealing; (f) spin-coated sample, after long solvent annealing; (h) drop-casted sample, freshly prepared. Reproduced with permission from Ref. [63]. Copyright 2017 American Chemical Society.

prolonged solvent annealing, as described below). These results could be interpreted with the concomitant occurrence of different domains, some of which had already reached a stable thermodynamic aggregate, while others were still evolving. In fact, after a more prolonged (several hours) solvent annealing, the global ECD spectrum recorded with the benchtop instrument (Figure 12e) assumed its definitive form: a negative couplet-like structure centered at about 435 nm, with the minimum around 490 nm. This is the most thermodynamically stable aggregation state reached under full equilibrium conditions, as further confirmed by SR-ECD*i* (Figure 12f): all the local spectra had the same shape and differed only in magnitude, due to a variation of the film thickness throughout the investigated surface area. Interestingly, the same shape was observed in both conventional ECD (Figure 12g) and SR-ECD*i* (Figure 12h) spectra of pristine drop-casted samples of D-Leu-PPE: under these conditions, the chiral polymer had enough time to reach its thermodynamically stable state.

The SR-ECD*i* technique was found very helpful in the investigation of thin films of chiral organic π-conjugated dyes characterized by significant non-reciprocal contribution in the global ECD spectrum. Among them, our group gave special emphasis to a 1,4-phenylene-thiophene oligomer functionalized with chiral 3,7-dimethyl-1-octyl chains:[64] the ECD spectrum of thin films prepared by spin coating showed a substantial non-reciprocal CP absorption, with g_{abs} (436 nm) of $-2.7 \cdot 10^{-2}$ for the sample with front illumination and $+2.8 \cdot 10^{-2}$ for the sample with back illumination. In particular, the reciprocal and non-reciprocal components of the spectrum (named, respectively,

CD$_{iso}$ and LDLB in the original publication) were calculated through the semi-sum and the semi-difference of the ECD spectra recorded for the two opposite sample orientations, resulting in a $\int |LDLB| / \int |CD_{iso}|$ ratio of 4.37. We now discourage the use of the term "isotropic CD" as a synonym for true CD of thin films, as these samples are intrinsically anisotropic. Further studies on the same sample were carried out in a following work by the SR-ECD*i* technique,[65] which clarified the aggregation pathways occurring in thin film fabrication. Local UV-Vis absorption and ECD spectra of a 10×10 grid matrix (0.5 mm step size) of a freshly-prepared spin-coated thin film were measured with a beam diameter of 0.5 mm (Figure 13a–b), and the values of absorption (at 433 nm) and ECD (at 436 nm) were then elaborated into 2D maps of the 10×10 grid area (Figure 13c–d). For each spot, the similarity factor (SF) index of the local ECD spectrum was calculated with respect to semi-sum (SF$_\Sigma$) and semi-difference (SF$_\Delta$) ECD spectra of the whole sample and reported as 2D maps (Figure 13e–f), showing that all the local ECD spectra were much more similar to the global LDLB (SF$_\Delta$ between 0.966 to 0.979) than to the global CD$_{iso}$ (SF$_\Sigma$ between 0.141 and 0.217). The conclusion of this study was that freshly prepared samples were trapped into a kinetic or metastable aggregation state, where the shear stress of spin coating favored the formation of anisotropic mesoscopic domains, each of them characterized by a strong interaction of their non-aligned LD and LB, responsible for a large non-reciprocal contribution.

A further interesting example of thin films of a chiral organic dye showing a substantial non-reciprocal ECD spectrum was a
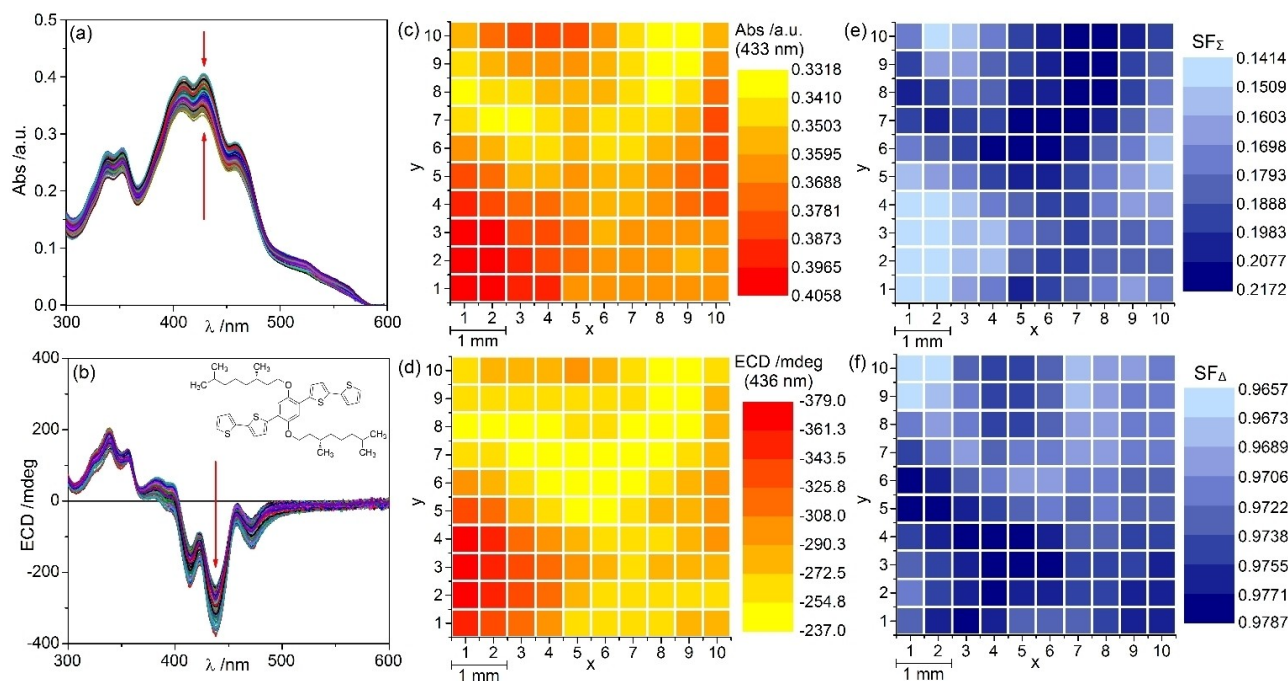

Figure 13. SR-ECD*i* investigation of freshly-prepared spin-coated thin films of a 1,4-phenylene-thiophene oligomer functionalized with chiral 3,7-dimethyl-1-octyl chains, performed on a 10×10 grid array area of 0.5 mm step size with a beam diameter of 0.5 mm. (a) Local UV-Vis absorption spectra and (b) local ECD spectra recorded for the 100 spots. 2D maps of: (c) absorbance intensity at 433 nm vs. x-y (red/yellow hues); (d) ECD intensity at 436 nm vs. x-y (red/yellow hues); (e) similarity factor index with respect to the global CD$_{iso}$ (SF$_\Sigma$) vs. x-y (blue hues); (f) similarity factor index with respect to the global LDLB (SF$_\Delta$) vs. x-y (blue hues). Adapted with permission from Ref. [65]. Copyright 2019 Centre National de la Recherche Scientifique (CNRS) and The Royal Society of Chemistry.

Chemistry–A European Journal

Review

doi.org/10.1002/chem.202301982

Chemistry Europe
European Chemical
Societies Publishing

benzo[1,2-*b*:4,5-*b'*]dithiophene-based oligothiophene bearing two enantiopure (*S*)-3,7-dimethyl-1-octyl alkyl chains:[66] drop-casted samples showed opposite ECD spectra for the two faces, with maximum dissymmetry factor g_{abs} value (at 299 nm) of $+1.8 \cdot 10^{-2}$ for the front and $-1.9 \cdot 10^{-2}$ for the back. Also in this case, the true CD (CD_{iso}) and non-reciprocal LDLB contributions were isolated by taking the semi-sum and the semi-difference of ECD spectra recorded with the two sample orientations, confirming a clear prevalence of the LDLB on the CD_{iso} (with a $\int |LDLB|/\int |CD_{iso}|$ ratio of 2.01). To further clarify the origin of these two contributions, the same sample was very recently studied by the SR-ECD*i* technique:[67] for both the front and back face a 31×31 grid matrix (0.1 mm step size) was mapped at 422 nm with a beam diameter of 0.05 mm, generating 2D maps of absorption (Figure 14a–b) and ECD (Figure 14c–d); the 2D maps of reciprocal CD_{iso} (Figure 14e) and non-reciprocal LDLB (Figure 14f) of the same grid array area were also evaluated. The SR-ECD*i* maps revealed spheroidal domains (diameter up to 2 mm) with strong local ECD signals, standing out from the background with weak dichroic signals, which were instead not visible in absorbance from unpolarised light. In particular, these domains could be considered responsible for the strong non-reciprocal term in the global ECD spectrum, while the background provides only a weak reciprocal contribution. These SR-ECD*i* measurements supported the hypothesis that the modest intrinsic true CD was generated by the first-order supramolecular chiral aggregates, while the large non-reciprocal LDLB was associated to the further organization of these supramolecular structures into locally anisotropic micro/mesoscopic domains. In each domain, the non-reciprocal LDLB term arose from the interaction of their LD and LB, whose principal axes are not aligned with each other. Since thin films were prepared without any operation which might impart a preferential molecular orientation, these domains had to be randomly oriented and both LD and LB averaged to zero over the whole film.

Our research group has successfully extended the use of SR-ECD*i* technique to other samples different from thin films:[68] local ECD spectra of a model microcrystalline solid (that is, chiral active pharmaceutical ingredient Finasteride) dispersed into KCl pellets were recorded at the Diamond Light Source B23 beamline, scanning a surface of 36 mm² with a step of 0.5 mm. Interestingly, local SR-ECD*i* spectra were very different from each other and from the ECD spectrum recorded for the whole pellet using a benchtop instrument. In this case, SR-ECD*i* offered a way to estimate anisotropic CD (ACD) associated with locally oriented microcrystals dispersed in the salt matrix.

In the last few years, the SR-ECD*i* set-up at Diamond Light Source B23 beamline was also used by other research groups for the study of thin films of organic dyes. Fuchter and co-workers have applied this technique for testifying the homogeneity of layers of a chiral polyfluorene derivative giving rise to a blue-phase endowed with extra-large ECD.[69] Pantos et al. have detected the formation of chiral and stable supramolecular assemblies with homogenous distribution in thin films of silicon phthalocyanines (SiPcs) bearing chiral lateral appendages (chiral naphthalenediimide derivatives or naproxen-based
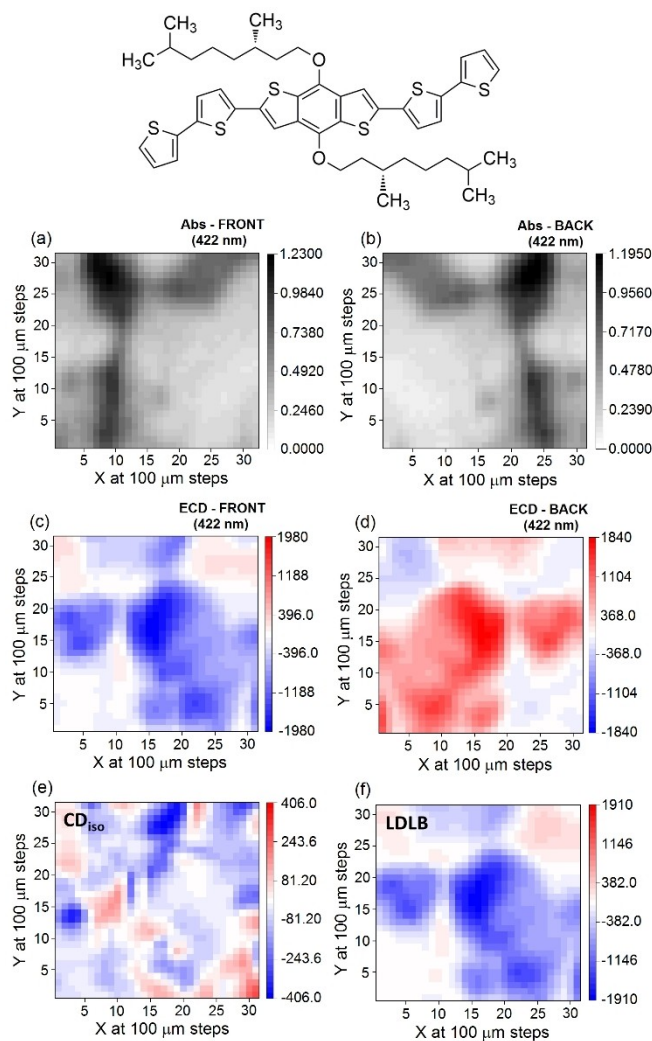

Figure 14. SR-ECD*i* investigation of freshly-prepared drop-coated thin films of a benzo[1,2-*b*:4,5-*b'*]dithiophene-based oligothiophene functionalized with chiral 3,7-dimethyl-1-octyl chains, performed on a 31×31 grid array area of 0.1 mm step size with a beam diameter of 0.05 mm. 2D maps of: UV-Vis absorbance intensity at 422 nm vs. x-y (black/grey/white hues) for the front face (a) and the back face (b); ECD intensity at 422 nm vs. x-y (red/white/blue hues) for the front face (c) and the back face (d); calculated true CD (CD_{iso}) and non-reciprocal LDLB (f) contribution at 422 nm vs. x-y (black/grey/white hues). Adapted from Ref. [67] under Creative Commons Attribution 4.0 International License, 2022 SCUT, AIEI, and John Wiley & Sons.

structures).[70] Amabilino and co-workers described a significant heterogeneity in the supramolecular arrangement of drop-casted thin films of a chiral diketopyrrolo[3,4-*c*]pyrrole dye, functionalized with enantiopure ethyl lactate groups through an ether linkage to the aryl backbone of the chromophore.[71] Finally, Siligardi's group has recently extended the application of SR-ECD*i* to a large number of thin films of achiral polyvinyl alcohol (PVA) doped with different amounts of enantiopure D-dopa, to assess the chiral homogeneity of thin film preparation with potential antimicrobial property.[72]

Very recently, our group proposed a new simple approach to ECD*i* of thin films of chiral organic dyes based on the *CPM configuration*.[73] The white light emitted from the lamp of a Zeiss Discovery V8 microscope was passed through a linear

Chemistry–A European Journal

Review

doi.org/10.1002/chem.202301982

Chemistry
Europe

European Chemical
Societies Publishing

polarizer and a birefringent quarter wave plate (QWP): by positioning the easy axis of QWP at $+45°$ or $-45°$ with respect to the linear polarizer filter, respectively right-handed and left-handed CP back-illumination was generated. The analysis of two different pictures of the same area taken with right-handed and left-handed CP light provided quantitative data of the CP-selective transmittance of the sample; the spatial resolution is on the micrometer scale and it is only limited by the magnification optics integrated in the microscope and by the diffraction limit. The CPM technique was applied to spin-coated thin films of two different chiral organic dyes: a 9H-carbazole-based oligothiophene (named Th$_2$-CBZ-Th$_2$) and a phenylene bisthiophenylpropynone (named PTPO), both functionalized with the 3,7-dimethyl-1-octyl chiral chain. The first one, characterized by a purely true ECD spectrum recorded with a benchtop spectropolarimeter,[16a] provided a very homogeneous texture in the CPM images; however, by comparing the two snapped pics, it could be clearly observed a slightly different hue, related to the differential transmission of the two CP light beams. The second one, characterized by an almost complete non-reciprocal CP absorption in the ECD spectrum recorded with a benchtop spectropolarimeter,[74] under CPM technique revealed a remarkable contrast with sharp polygonal boundaries among regions which appeared more transparent to left-handed CP light and other ones to right-handed CP light; in other words, domains that were bright yellow when the film was backlit with left CP light, became darker when it was backlit with right CP light, and vice-versa. In the case of Th$_2$-CBZ-Th$_2$, an identical ECD spectrum was found for every point of the film; for PTPO the ECD measured on a large surface with a standard spectropolarimeter was the result of an average of very different values, not only in magnitude but even in sign. Despite its simplicity, this technique can be successfully applied only for thin films of chiral organic dyes characterized by intense g_{abs} values in the global ECD spectrum.

As already described in the Introduction, the study of chiroptical properties in thin films of organic dyes is typically more complex than solutions: the experimental ECD signals is the sum of several different terms, including parasitic contributions due to the concomitant occurrence of circular and linear anisotropies (linear dichroism, LD; linear birefringence, LB; circular birefringence, CB). Unfortunately, most of the above mentioned ECDi set-up suffered (in some cases more explicitly than others) from this issue. The possibility to repeat ECDi measurements upon sample rotation and flipping is a viable solution, although it could be difficult to scan exactly the same area. Therefore, the development of spatially resolved Mueller matrix techniques represents definitely an important strategy for mapping and disentangling circular and linear anisotropies in thin films, and we shall briefly discuss them in the final part of this section.

Despite spatially resolved Mueller matrix techniques began to be adopted in the study of thin films of chiral organic dyes only in the last years, they started to be of interest for biological specimens several years ago.[75] The first full Mueller matrix determination through polarimetry imaging was reported in 1999 for ophthalmology applications. Polarization modulated scanning laser microscopy mapped the retinal and pupil planes of the human eye in reflection.[76] This technique required anyway to carry out 16 different measurements, although characterized by a short time, to determine all the Mueller matrix elements. However, a remarkable advantage is given by the possibility to avoid the presence of any moving part in the instrumental setup.

In the following years, thanks to the significant reduction of images blur noise and the possibility to study different levels of thick samples (typically having thickness $> 1\ \mu m$), confocal microscopy became of particular interest in the Mueller matrix tomographic investigation of biological systems. Initially, it was adopted in the reflection mapping for retinal diagnosis. Herein, the use of two Pockel cells for the outcoming and incoming polarization modulations led to a better signal-to-noise ratio, thanks to the automation of multiple consecutive accumulations.[77] Throughout the years, there was a tremendous development in Mueller matrix imaging dedicated to diseases diagnosis, such as glaucoma,[78] and biological samples, such as stretched starch[79] and diluted milk,[80] with a relevant increase in the automation of the instrumental components to be moved.

However, the most significant improvement in Mueller matrix microscopy performances occurred in 2012, when Arteaga et al. developed a new setup with four photoelastic modulators and no moving parts able to simultaneously afford all the 16 Mueller matrix elements, without the need to carry out a measurement for every polarization state.[81] This was possible thanks to an analysis in the frequency domain of the time-dependent intensity of the light beam. An alternative, which is anyway determining all the Mueller matrix elements simultaneously, is offered by a setup adopting two rotating compensators as encoding/decoding system.[82]

Later, an instrumentally simpler but less performant setup was proposed as further alternative. Instead of two rotating compensators, just one was involved, allowing the determination of the first three elements of the outcoming Stokes vector with four measurements, that is the same of defining the first three rows of the medium's Mueller matrix.[83] Such strategy is suitable for nondepolarizing samples and fails otherwise in the full determination of the Mueller matrix with depolarizing samples.

Despite all the improvements described above for Mueller matrix imaging techniques, the possibility of recording the matrix elements over a spectral range was still lacking. This gap was filled through synchrotron radiation as the light source, exactly as it is for SR-ECDi. The coupling of an already developed instrumental setup and B23 beamline synchrotron radiation gave birth to synchrotron radiation Mueller matrix polarimetry imaging (SR-MMPi).[62] SR-MMPi was the first Mueller matrix imaging technique to be adopted in the mapping of chiral supramolecular aggregates of organic dyes in thin film, a technique discussed already for diketopyrrolo[3,4-c]pyrrole dye.[84] However, in this work, the authors preferred to focus exclusively on the ECD term extracted from SR-MMPi measurements. More recently, SR-MMPi was employed by Pantos and

Chemistry–A European Journal

Review

doi.org/10.1002/chem.202301982

Chemistry Europe
European Chemical
Societies Publishing

co-workers in the mapping of vortex-induced chiral J-aggregates of a cyanine dye in thin film.[85]

3. Circularly Polarized Luminescence Imaging (CPL*i*)

The use of CPL spectroscopy in the characterization of thin films of chiral organic dyes provides information by interrogating the molecules in their excited states, which is then complementary to that obtained by ECD (as well as by MMP and MMSE). Structure heterogeneity and local polymorphism could be responsible for different contributions to the global CPL spectrum; therefore, recognizing and identifying them is mandatory for the efficient application of chiral emissive materials as active layers in CP-OLED devices.

Compared to the ECD*i* techniques described in the previous section, the development of dedicated instrumentations for CPL*i* measurements started more recently: the first example of a CPL microscope was developed in 2010 by Favorskiy and co-workers,[86] although it was used to study lateral charge and spin diffusion in inorganic semiconductors. In particular, the CPL microscope was a modified Nikon Optiphot 70, schematically depicted in Figure 15. The photoexcitation of the sample
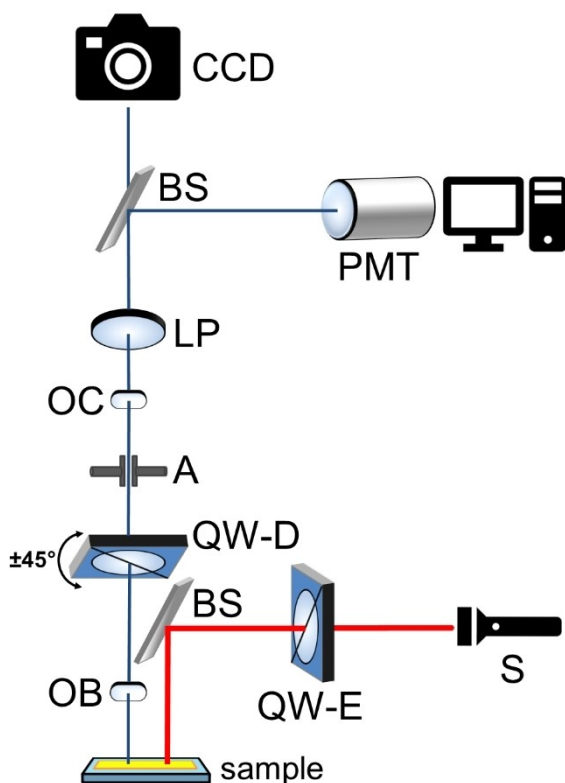

Figure 15. Schematic representation of the CPL microscope instrumentation developed in 2010 by Favorskiy and co-workers. Legend: S, laser excitation source; QW-E, quarter wave plate in excitation; BS, beam splitter; OB, objective; QW-D, quarter wave plate in detection; A, analyzer; OC, ocular; LP, linear polarizer filter; CCD, CCD camera; PMT, fiber-coupled spectrometer. Adapted with permission from Ref. [86]. Copyright 2010 American Institute of Physics.

was made possible by a laser excitation source, mounted in a 90° geometry with respect to the sample holder; the laser beam, passing through a quarter wave plate, reached a beam splitter which deflected it towards the sample. The light emitted by the thin film, passing through a second quarter wave plate and a linear polarizer filter, was then sent to a CCD camera for observing sample images or to a fiber-coupled spectrometer for recording CPL spectra thanks to a second beam splitter. By rotating the easy axis of the quarter wave plate in detection by $\pm 45°$ with respect to the linear polarizer, the left- and right-handed components of the emitted light were alternatively acquired. Although this first example of CPL*i* instrumentation, attributable to the *CPM configuration*, was not applied to chiral organic dyes and allowed only limited spatial resolution, such technique was simple and, in practice, equivalent to taking images on a standard laboratory optical microscope.

A few years later, a new CPL microscope belonging to the *LCS configuration* was developed by Kawai and co-workers for the investigation of chiral lanthanide(III) complexes in single crystals.[87] A continuous wave GaN laser (375 nm, 7 mW) was used as the photo-excitation source, while an objective lens was mounted for focusing the excitation beam and correcting the emitted light from crystal samples, which then passed through a photoelastic modulator (PEM) operating at 50 kHz frequency. The CP component of the emitted light was then converted into linearly polarized light and detected by a photomultiplier tube after passing through a linearly polarized cubic prism for analyzing CPL signals. The sample holder was composed of two-axis rotational stages and two linear stages, while focusing was confirmed by means of a CCD camera, optically inserted and removed by moving a mirror between a dichroic mirror and PEM.

In 2013 Kawai's group used the same instrumentation for the characterization of drop-casted samples of *trans*-1,2-bis(perylenediimide)-cyclohexane:[88] to the best of our knowledge, this is the first application of CPL*i* measurements on thin films of chiral organic dyes. Although these fluorescent samples had an apparent macroscopically uniform and homogeneous morphology, showing maximum luminescence dissymmetry factor g_{lum} value of $+0.035$ at 650 nm for the (*S,S*) enantiomer, AFM images suggested a more complex structure, consisting of helical networks of fibrous assemblies. For this reason, CPL*i* measurements were performed to confirm the consistency of chiroptical signals at different points of the same film: fluorescence, CPL and g_{lum} values were simultaneously monitored by mapping a 40×40 μm² area at a gap distance of 4 μm. In particular, the g_{lum} 2D-map recorded for the (*S,S*) enantiomer consistently showed positive values (Figure 16): despite some differences in intensity from each spot to another, the values distribution showed a peak between 0.02 and 0.03, demonstrating the uniformity of CP emission of the aggregated structures on the surface.

A further interesting application of this CPL microscope was reported in 2018 by the same research group, who synthesized a new photoluminescent pyrene derivative containing two chiral imidazole moieties (named Im₂Py), able of self-assembling into chiral stacks upon coordination to Zn²⁺ cations in
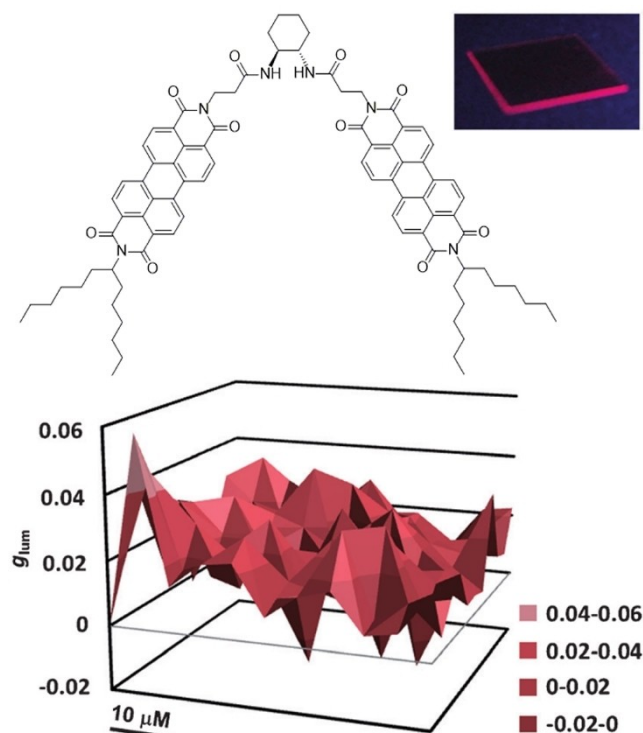
Chemistry–A European Journal

Review
doi.org/10.1002/chem.202301982

Chemistry Europe
European Chemical
Societies Publishing

Figure 16. CPL*i* measurements on thin films of (1*S*,2*S*)-*trans*-1,2-bis(perylenediimide)-cyclohexane prepared by drop casting technique: dissymmetry factor g_{lum} 2D-map recorded by mapping a 40×40 μm^2 area at a gap distance of 4 μm. Adapted with permission from Ref. [88]. Copyright 2013 John Wiley & Sons.

acetonitrile solution.[89] Interestingly, Im$_2$Py displayed no chiroptical signals in absence of metal ions, while an intense CPL took place upon self-assembly with Zn^{2+}. Although they were performed in solution, in this study CPL*i* measurements were used as a smart sensing method for object identification, discriminating between the signal of a target analyte (Zn^{2+} cations) and that of non-target species.

In 2014, Vacha et al. reported the application of CPL*i* measurements to the characterization of local chiral supramolecular structures in drop-casted and spin-coated thin

films of poly[(9,9-dioctylfluorenyl-2,7-diyl)-*co*-bithiophene] (F8BT): although it is an achiral polymer, the formation of chiral aggregates was induced via solvent chirality transfer, in the presence of (*R*)- or (*S*)-limonene during the solution aggregation process just before thin film fabrication.[90] In this case, the instrumental set-up was based on a home-built confocal fluorescence microscope (Figure 17a). The thin film sample was excited with a continuous wave laser (488 nm) through an oil-immersion objective lens, while the emitted light from the sample passed through an electro-optical modulator, which applied alternately a +90°/−90° phase shift. As a result, circular polarization was converted into two alternating orthogonal linear polarizations, only one of which passed the linear polarizer placed behind the electro-optical modulator and reached an avalanche photodiode. A bandpass filter placed between the linear polarizer and the photodiode was used to selectively detect the emission in the region between 500 and 550 nm. In this experimental set-up, which can be associated with the *CPM configuration*, the most critical elements in the detection path are the dielectric mirror below the objective lens and, above all, the dichroic mirror, which caused severe distortion of circular polarization when used at its designed incident angle of 45°; to avoid this problem, such mirror was used at an incident angle of only 3°. CPL microscopy images of thin films revealed quite irregular structures, having a size of ~10 μm in the case of drop-casted samples (Figures 17b–c) and of 1–2 μm in the case of spin-coated samples (Figures 17f–g); at the same time, the g_{lum} distributions obtained from 80 different spots for the *R* and *S* aggregates of drop-casted (Figures 17d–e) and spin-coated thin films (Figures 17h–i) exhibited local g_{lum} values very different from each other, as well as from the g_{lum} value obtained via standard CPL spectroscopy for the whole sample. The authors explained these differences hypothesizing that local g_{lum} values could be distorted by additional phase retardation along the optical path in the sample, thus containing little information on the circular polarization state of the emitted light itself. Therefore, only the difference $\Delta\bar{g}$ between the centers $\bar{g}$ of g_{lum} distributions for the *R* and *S* forms (0.022 for drop-casted samples; 0.016 for spin-coated samples) truly reflected the intrinsic CPL phenomenon resulting from the
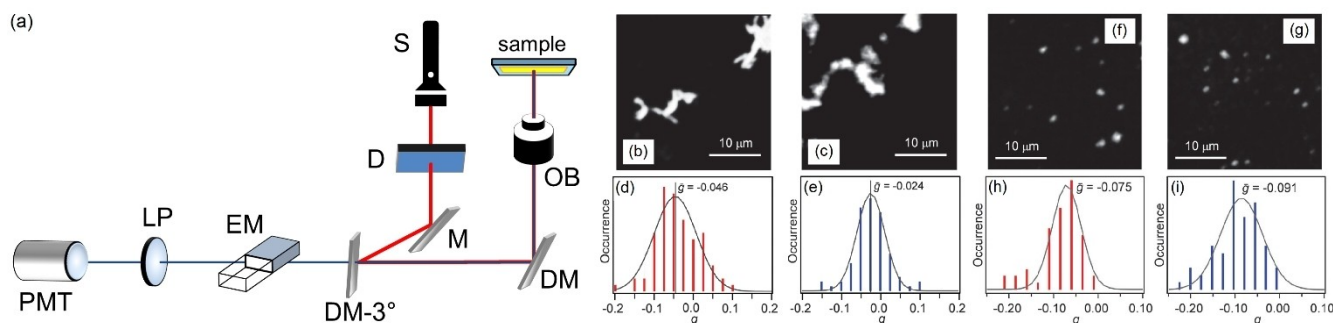

Figure 17. (a) Schematic representation of the CPL microscope instrumentation developed in 2014 by Vacha et al. Legend: S, excitation source; D, depolarizer; M, mirror; DM-3°, dichroic mirror at 3°; DM, dielectric mirror; OB, objective lens; EM, electro-optical modulator; LP, linear polarizer; PMT, detector. CPL*i* characterization of thin films of F8BT prepared by drop casting: (b) confocal fluorescence images of the *R* aggregates and (c) of the *S* aggregates; (d) distribution of the g_{lum} values measured from 80 spots of the *R* aggregates and (e) of the *S* aggregates. CPL*i* characterization of thin films of F8BT prepared by spin coating: (f) confocal fluorescence images of the *R* aggregates and (g) of the *S* aggregates; (h) distribution of the g_{lum} values measured from 57 spots of the *R* aggregates and (i) from 63 spots of the *S* aggregates. Adapted with permission from Ref. [90]. Copyright 2014 the PCCP Owner Societies.

Chemistry–A European Journal

Review

doi.org/10.1002/chem.202301982

**Chemistry
Europe**
European Chemical
Societies Publishing

chirality of the excited state. Thus, the smaller $\Delta\bar{g}$ value found for the smaller aggregates of spin-coated thin films was not due to size confinement of the chiral structure, but rather to the consequence of a less ordered structure of such aggregates. The present study well-evidenced how data analysis and interpretation in the CPL imaging of thin films must be done with the utmost care.

As already described in the previous section, in 2022 Lenzer and co-workers developed a new instrumentation for both ECD*i* and CPL*i* measurements, attributable to the *CPM configuration*, based on the same wide-field microscopy reaching a spatial resolution of ~500 nm.[58] The set-up for CPL microscopy involved a 365 nm photo-excitation source (emitted by a Xenon lamp-monochromator combination) coupled with the wide-field microscope by a quartz fiber, in order to excite the sample through the microscope objective. The luminescence of the thin film passed through a long-pass filter and a quarter wave plate, then it was divided by a beam-splitter; one part passed through a polariser and was detected by the CCD camera to obtain photoluminescence images, while the other one passed through another polariser and was then focused by a quartz lens into an optical quartz fiber connected to a spectrograph. Spatially resolved CPL images at selected wavelengths and CPL spectra of local spots were obtained from two measurements, in which the easy axis of the quarter wave plate was set at either $+45°$ or $-45°$ with respect to the polariser axis. Compared to ECD*i* images recorded with the same instrument, the obtained CPL*i* images were more blurred and had less contrast, probably due to the longer integration time. In a first work, the authors applied this microscopy set-up for the investigation of the supramolecular chirality of excited states in spin-coated thin films of a chiral co-polymer *c*-PFBT:[58] interestingly, the CPL and g_{lum} images recorded for a 80×60 μm² area with a 500 nm spatial resolution (Figures 18a–b) revealed the same island-type areas observed in the ECD*i* maps, whose size was very similar to the dimensions of fiber-type and aggregated spherulite arrangements described by Di Nuzzo et al.[91] and Lakhwani and et al.[92] for thin films of c-PFBT by conventional microscopy techniques. The values collected in the g_{lum} map were processed into a histogram (Figure 18c), described by a Gaussian distribution, with $g_{lum}^{max} = -0.29 \pm 0.02$, in good agreement with the value measured on the whole sample by a benchtop CPL instrumentation. In addition to spatially resolved images at a selected wavelength, the CPL microscope recorded local spectra from 450–750 nm (Figure 18d).

In a following study, Lenzer and co-workers applied the same CPL microscope to the investigation of the chiral induction exerted by two different helicene-type additives in thin films of the achiral luminescent co-polymer F8BT;[60] in particular, CPL*i* measurements helped clarify the origin of the large induced chiroptical response in such films. CPL microscopy images of spin-coated thin films of F8BT blended with both enantiomers of the unbridged helicene-type additive 2,2′-dimethoxy-5,5′,6,6′-tetrahydro-1,1′-bidibenzo[*c,h*]acridine **A** (Figures 19a–b) revealed a strong chiral induction of opposite sign (testified by the blue and red colours). An island-like granular texture was observed, similar to the corresponding ECD*i* images described in the previous section,
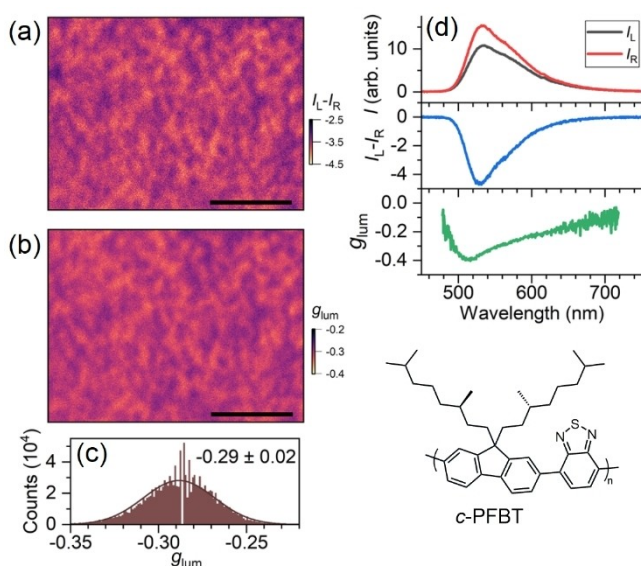

Figure 18. (a) CPL microscopy image and (b) g_{lum} microscopy image of spin-coated thin films of the chiral co-polymer *c*-PFBT, recorded for a 80×60 μm² area with 500 nm spatial resolution (excitation: 365 nm; scale bar: 25 μm). (c) Distribution of the g_{lum} values collected in the panel b for the 80×60 μm² area of the sample. (d) Photoluminescence of left-handed CP light (black line) and right-handed CP light (red line), CPL (blue line) and g_{lum} (green line) spectra recorded in the 450–750 nm wavelengths range for the same 80×60 μm² area of the sample. Reproduced from Ref. [58] under Creative Commons Attribution 4.0 International License, 2022 Springer Nature.

even if they were more blurred due to reflection and scattering of the isotropic luminescence from polymer domain boundaries, as well as to the influence of vibrations of the microscopy instrumentation during the integration time (several seconds). By using the methylene-bridged analogue **B** of the helicene-type additive, CPL microscopy images revealed a less intense chiral induction, testified by the pale blue and pale red colours (Figures 19c–d). It is worth emphasizing that helicene-type chiral additives gave no contributions to the spectral features of CPL images, as their photoluminescence and CPL signals occurred at shorter wavelengths with respect to those of F8BT co-polymer.

For the sake of completeness, at the end of this section it is also important to briefly mention recent CPL*i* investigations on lanthanide(III) complexes with chiral organic ligands. In 2020, Iwamura and co-workers reported the application of the achiral [Eu(pda)₂]⁻ (pda: 1,10-phenanthroline-2,9-dicarboxylate) complex as a luminescent probe in agar gels containing chiral α-amino acids (arginine or histidine), in order to perform CPL*i* measurements using a laboratory-built microscopic CPL spectroscopic system depicted in Figure 20a.[93] In this experimental set-up, which falls under the *LCS configuration*, the samples were typically excited in the range of 340–400 nm by a Hg-Xe lamp, whose beam was focused through a dichroic mirror and objective lens on the sample holder. The emitted light, collected by the same lens, was then reflected by a different dichroic mirror to an iris diaphragm, then transmitted to a photo-elastic modulator; photons corresponding to the emitted left- and right-handed CP light were selectively counted by synchronizing with the photo-elastic modulator. Finally, pho-
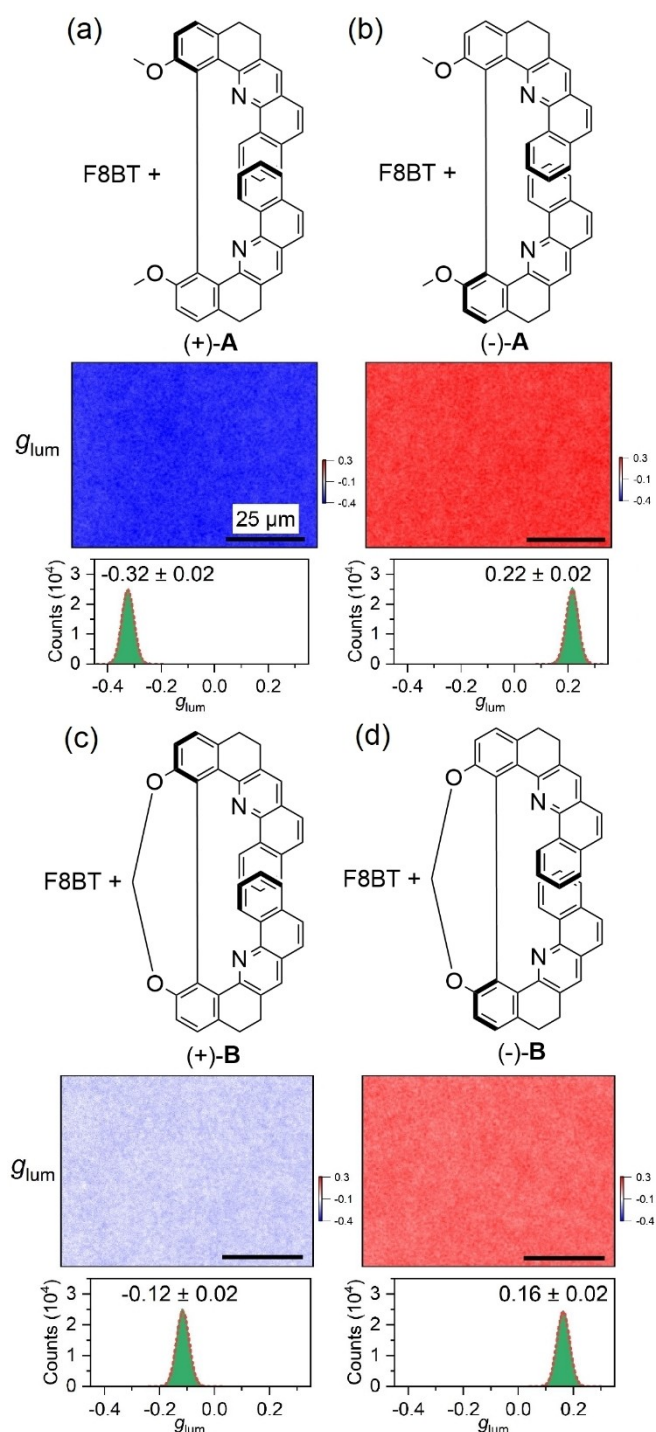
Chemistry–A European Journal

Review

doi.org/10.1002/chem.202301982

Chemistry Europe
European Chemical
Societies Publishing

Figure 19. Luminescence dissymmetry factor g_{lum} microscopy images, recorded for a 80×60 µm² area with 500 nm spatial resolution (excitation: 365 nm; scale bar: 25 µm), and corresponding values distributions measured for spin-coated thin films of achiral co-polymer F8BT blended with helicene-type additives: (a) F8BT/(+)-**A**; (b) F8BT/(−)-**A**; (c) F8BT/(+)-**B**; (d) F8BT/(−)-**B**. Adapted from Ref. [60] under Creative Commons Attribution 4.0 International License, 2022 John Wiley & Sons.

tons were dispersed by a monochromator and detected by a photomultiplier tube. Samples of agar gels with an inhomogeneous distribution of both D- and L-amino acids and a homogeneous dispersion of $[Eu(pda)_2]^-$ were prepared; then,

the induced CPL of the achiral europium complex exerted by the chiral α-amino acids was recorded by spatially resolved CPL*i* measurements, scanning a 2×2 mm area around the boundary between D- and L-amino acids. Interestingly, significant difference between the CPL images of arginine-doped (Figure 20b) and histidine-doped agar gels (Figure 20c) was found: a high-contrasted clear boundary was observed in the former case, while the border was poorly defined and weak in the latter case. The different CPL*i* 2D-maps suggested a difference in the mechanism of chiral induction of the two α-amino acids: arginine preferred the organization into homo-associated species $[Eu(pda)_2]^- \cdot (L\text{-Arg})_2$ or $[Eu(pda)_2]^- \cdot (D\text{-Arg})_2$ to hetero-associated species $[Eu(pda)_2]^- \cdot (L\text{-Arg})(D\text{-Arg})$; conversely, histidine self-assembled mostly into hetero-associated species $[Eu(pda)_2]^- \cdot (L\text{-His})(D\text{-His})$. The boundary mixing of D- and L-arginine due to molecular diffusion did not result in a decrease of CPL signals (high-contrasted borders). However, this was observed for D- and L-histidine (blurred borders).

The most important results in the development of microscopy instrumentation for spatially resolved CPL*i* measurements on chiral lanthanide(III) complexes have been obtained by Pal, Parker and co-workers. In 2016 they reported the adaptation of an epifluorescence microscope for CPL analysis,[94] performed by simply retrofitting the detection pathway with a quarter wave plate, responsible for the conversion of the emitted CP light into linearly polarised light, and a selector for two orthogonally oriented linear polarizers, allowing the selection and differentiation of vertically and horizontally polarised linear light. This proof-of-concept instrumentation, clearly belonging to the *CPM configuration*, was successfully used in the investigation of both enantiomers of a chiral lanthanide complex ($[EuL^1]$, Figure 21) with strong CPL emission ($g_{lum} = \pm 0.11$) absorbed onto an optical brightener-free paper test substrate,[94] thus demonstrating that the enantiomers of EuL^1 could be spatially discriminated by their CPL emission profile. In a following study, the authors applied the same CPL*i* instrumentation for living-cell imaging of the enantioselective distribution of three chiral europium(III) complexes: for each of them, a highly selective mitochondrial localisation of the Λ enantiomer in NIH 3T3 and MCF7 cells was observed, while a predominant lysosomal localisation was found in the case of the Δ enantiomer.[95] Such epifluorescence CPL microscope was considerably faster than all the other previously described microscopes based on electro-optical modulator or photo-elastic modulator (that is, 2 min vs. 40 min total image acquisition); however, it required sequential manual selection of CPL detection channels, which is impractical for sub-cellular imaging, where high space-temporal resolution is mandatory to track chiral interactions in real time. A fast CPL microscope, but at the same time able of simultaneously measuring left- and right-handed CPL could represent a step change in technological capability, opening up new opportunities to study chiral molecular interactions. For this reason, very recently Pal, Parker and co-workers reported the development of a CPL laser scanning confocal microscopy (CPL-LSCM), allowing very fast CPL*i* measurements thanks to the simultaneous acquisition of left and right-handed CPL images with a spatial resolution of 100×100 µm in 9 s.[96] Sample

Chemistry–A European Journal

Review

doi.org/10.1002/chem.202301982

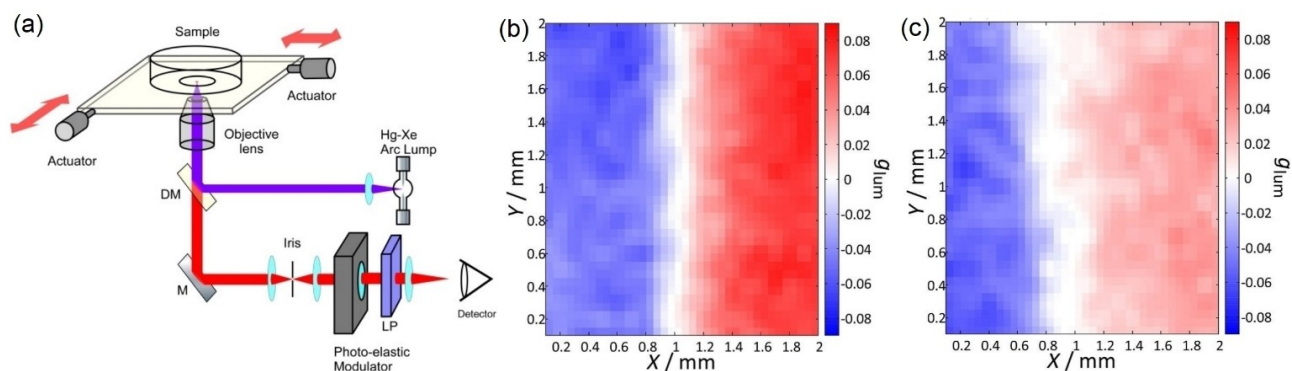**Chemistry Europe**
European Chemical
Societies Publishing

Figure 20. (a) Schematic representation of the laboratory-built microscopic CPL spectroscopic system developed in 2020 by Iwamura and co-workers. Microscopy g_{lum} images (at 591.4 nm) of agar gel containing chiral arginine (b) or histidine (c) amino acid and achiral [Eu(pda)$_2$]$^-$ complex. For each panel, the L-amino acid is dissolved in the right part of the map, while the D-amino acid in the left part; [Eu] = 0.1 mmol/dm^3, λ_{ex} = 340–400 nm). Reproduced with permission from Ref. [93]. Copyright 2020 John Wiley & Sons.
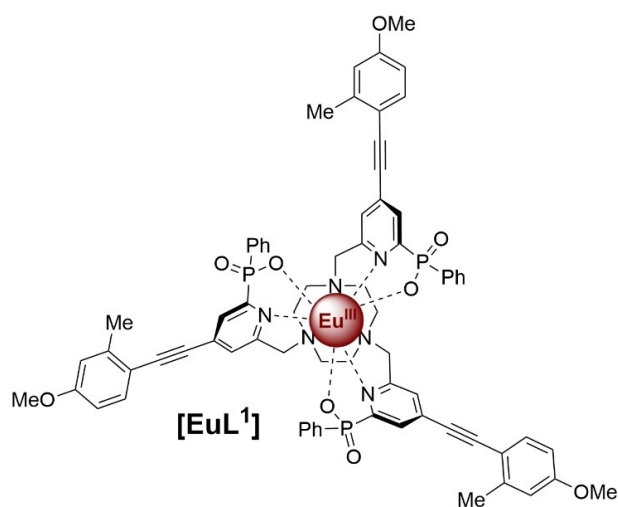

Figure 21. Structure of europium[1,4,7-tris((4-[2-(4-methoxy-2-meth-ylphenyl)ethynyl]-6-[carboxy(phenyl)phosphoryl]pyridin-2-yl}methyl)-1,4,7-triazacyclononane] [EuL^1], investigated by Pal, Parker and co-workers in their works on CPLi with a epifluorescence CPL microscope and a CPL laser scanning confocal microscope (CPL-LSCM).

photo-excitation was carried out at 355 nm with a Nd:YAG (3rd harmonic) laser, while the luminescence beam emitted from the sample coming out of the laser scanning confocal microscopy hit an external CPL analysis module, consisting of a bandpass filter, which selected the wavelength of interest, a quarter wave plate, which converted left- and right-handed CP light into orthogonal linearly polarised light, and a beam splitter. The two generated linear polarised beams, corresponding to left or right CPL, passed through a linear polarizer and, through dedicated focusing lens, finally arrived to photodiode detectors. This new CPL microscope was tested on the same [EuL^1] complex (Figure 21) used by the authors in their previous work: not only in the enantioselective differential chiral contrast of both Λ and Δ enantiomers deposited onto a glass substrate, but also in their enantioselective localisation into lysosome or mitochondria in living NIH 3T3 cells.

4. Vibrational Circular Dichroism Imaging (VCD*i*)

Recent VCD*i* experiments have enlarged the study of the local structure in thin films.

The first VCD*i* measurement was carried out in 2017 by Nafie and co-workers,[97] who fabricated a VCD sampling assembly with either 3 mm or 1 mm of spatial resolution: an XY-translation stage was used to record local spectra of different spots, producing IR and VCD maps of the sample, while a rotating sample stage in the presence of a dual photoelastic modulator suppressed the artifacts due to linear anisotropies. Such VCD microsampling instrumentation, which falls under the *LCS configuration*, was used for mapping insulin fibrils and a lysozyme thin film. The VCD*i* map of the first sample revealed changes in the local intensities which did not match with the corresponding spots of the IR map, thus indicating different degrees of supramolecular chirality of the fibrils in the various spatial regions. In the other sample, in addition to different degrees of supramolecular chirality, a reversal of the net fibril chirality was observed.

In 2021, Bhargava et al. proposed the development of a different set-up for VCD*i* studies, based on a custom-built quantum cascade laser (QCL)-equipped microscope (that is, *CPM configuration*).[98] As depicted in Figure 22a, the set-up was based on a custom-built stage-scanning microscope design enabling fast and point-by-point image acquisition: the QCL source emitted an IR laser beam (tuneable between 770 and 1940 cm^{-1}), which passed through a linear polarizer and a photoelastic modulator (PEM). The first device ensures a consistently polarized optical beam, while the latter allowed for a modulation between left-handed and right-handed CP light. The beam was then focused through objective lens on the sample, and the transmitted signal was finally focused onto a cryogenic photovoltaic HgCdTe detector. Such instrumentation was applied for site-specific chirality mapping of biological tissue samples (colon tissue cores) with various grades of malignant (Figure 22b): this investigation offered some insight into future possibilities of examining small, localized changes in
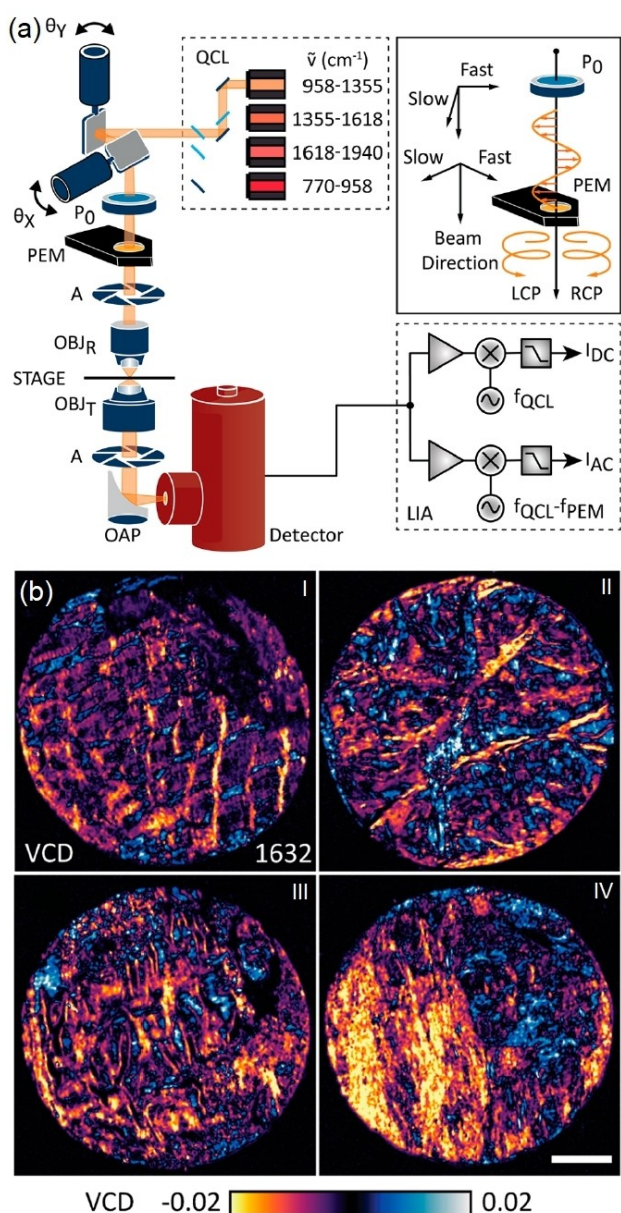
Chemistry–A European Journal | Review
doi.org/10.1002/chem.202301982

Chemistry
Europe
European Chemical
Societies Publishing

Figure 22. (a) Schematic representation of the QCL-VCD microscope developed in 2021 by Bhargava et al. Legend: QCL, quantum cascade laser source; P_0, linear polarizer filter; PEM, photoelastic modulator; A, aperture; OBJ_R, objective refractive lens; STAGE, sample holder; OBJ_T, objective transmission lens; OAP, off-axis parabolic mirror; LIA, lock-in amplifier. Detection occurred at multiple demodulation frequencies, namely f_{QCL} and $f_{QCL} - f_{PEM}$, enabling isolation of standard IR absorbance and VCD signals, respectively. (b) VCD*i* maps at 1632 cm^{-1} of four samples of colon tissues with normal (panel I: I5) and various grades of malignant (panel II: B12, panel III: G5, panel IV: B6); all scale bars are 250 μm. Reproduced with permission from Ref. [98]. Copyright 2021 American Chemical Society.

tissues that have major implications for systemic diseases and their progression.

Simultaneously with this work of Bhargava et al., Sato, Koshoubu and co-workers also reported the development of a very similar QCL-VCD microscope for spatially resolved VCD*i* measurements (also in this case falling into the *CPM config-uration*), although working in a smaller wavenumber range (1500–1740 cm^{-1}).[99] Once again, thin film samples have not

been investigated here: only KBr pellets containing α-amino acids,[100] or biological sample (hind wing of *Anomala albopilosa*).[101] In the last case, VCD*i* measurements were very helpful in clarifying the distribution of proteins, including their supramolecular structures, thanks to the analysis of amide I and II VCD bands: the 2D maps revealed that such hind wing consisted of local domains of proteins with different secondary structures: i) an α-helix, in one part of the membrane; ii) a hybrid of α-helix and β-sheet, in another part of the membrane; iii) a random coil, in a vein.

Although not yet applied to thin films, VCD*i* technique seems promising in this field too. In contrast to ECD, VCD may be directly applied to non-chromophoric compounds, although this may represent a minor advantage in the context of optoelectronic materials which intrinsically contain conjugated moieties. On the other hand, VCD has complementary structural sensitivity to ECD and may afford information about different structural details.[102] Furthermore, the well-developed IR micro-scopy instrumentation lends itself for a facile implementation of VCD*i*.

5. Conclusions

The ability of identifying and structurally characterizing the aggregated states in thin films of chiral organic π-conjugated materials on widely different length-scales is a key strategy for optimizing their performance as active layers for innovative optoelectronic applications. Optical and electron microscopy techniques can be successfully used for the characterization of thin films morphology with a resolution down to 10–100 nm scale, while they can hardly provide insight into the intimate supramolecular organization on the 1–10 nm scale. On the other hand, chiroptical spectroscopies typically provide geo-metrical information about the first level of chiral supramolecular organization at the nanometer scale, although with no spatial resolution. The recent development of spatially resolved chiroptical spectroscopies allows one to combine the advantages of both techniques: in the last fifteen years, they have represented a new valuable tool for mapping and disentangling local supramolecular structures in thin films of chiral organic dyes.

In the present review we gave a critical and up-to-date overview of the techniques developed for spatially resolved chiroptical investigation, giving special emphasis to their application to thin films of chiral organic dyes. In particular, we found that all the above described experimental set-ups for spatially resolved chiroptical spectroscopies could be grouped into two different types of schemes: i) the *LCS configuration*, where the light beam is focused into a small point in order to collect the signal from that point only, followed by systematic displacement of the sample on a XY stage to map its surface and gain imaging; ii) the *CPM configuration*, where full images of the whole sample can be obtained at once, by introducing the polarizing elements in the fundamental design of a micro-scope. This is more clearly highlighted in Table 1, where we summarized all the relevant information on the above-men-

Table 1. Overview of all the experimental set-ups developed for spatially-resolved chiroptical spectroscopies.

Name of the technique	Authors	Type of chiroptical measurement	Type of configuration	Analyzed samples	References
ECD microscope	Maestre and Katz	ECD*i*	LCS	several biological samples	[31],[32],[33],[34]
visible light ECD microscope	Kahr et al.	ECD*i*	CPM	several organic and inorganic crystals	[37],[38],[39]
home-built ECD microscope	Watarai et al.	ECD*i*	hybrid system	drop-casted thin films of cationic (TMPyP)/DNA complex	[41]
TPF scanning confocal microscopy for ECD*i*	Finazzi et al.	ECD*i*	CPM	thermally annealed spin-coated thin films of poly[9,9-bis((3S)-3,7-dimethyloctyl)-2,7-fluorene]	[42]
PM-SNOM	Narushima, Okamoto et al.	ECD*i*	LCS	2D chiral metal nanostructures; ribbon-like nanosized J-aggregates of TPPS$_3$	[45],[45–46],[47]
discretely modulated circular polarization	Narushima, Okamoto et al.	ECD*i*	LCS	chiral gold nanostructures; microporous chiral MOF; chiral plasmonic materials; κ-NCS crystals	[48],[49],[50],[51]
micro-spot ECD*i*	Percec et al.	ECD*i*	LCS	thin films of racemic perylene bisimides	[52]
micro-spot ECD*i*	Choi et al.	ECD*i*	LCS	achiral liquid crystal into chiral nanoporous films	[54]
Hamamatsu Photonics ECD microscope	Yamaguchi et al.	ECD*i*	CPM	pseudoenantiomeric aminomethylene-helicene oligomers (solution samples)	[55],[56]
custom-built set-up for ECD*i*	Hud et al.	ECD*i*	LCS	organic (nucleobase mimics) hydrogels	[57]
wide-field microscopy	Lenzer et al.	ECD*i*, CPL*i*	CPM	spin-coated thin films of c-PFBT; thin films of F8BT blended with helicene-type additives	[58],[60]
SR-ECD*i*	Di Bari, Siligardi et al.	ECD*i*	LCS	thin films of chiral D-Leu-PPE; 1,4-phenylene-thiophene oligomer; BDT-based oligothiophene	[63],[65],[67]
SR-ECD*i*	Siligardi et al.	ECD*i*	LCS	thin films of chiral polyfluorene; chiral SiPcs; chiral DPP; achiral PVA + D-dopa	[69],[70],[71],[72]
circularly polarized microscopy	Di Bari et al.	ECD*i*	CPM	thin films of chiral organic dyes	[73]
CPL microscope	Favorskiy et al.	CPL*i*	CPM	inorganic semiconductors	[86]
CPL microscope	Kawai et al.	CPL*i*	LCS	lanthanide complexes crystals; drop-casted film of trans-1,2-bis(perylenediimide)-Cy; Im$_2$Py/Zn^{2+} (solution)	[87],[88],[89]
CPL microscope	Vacha et al.	CPL*i*	CPM	thin films of F8BT fabricated via solvent chirality transfer (in the presence of (R)- or (S)-limonene)	[90]
laboratory-built microscopic CPL spectroscopic system	Iwamura et al.	CPL*i*	LCS	[Eu(pda)$_2$]$^-$ in agar gels containing chiral α-amino acids	[93]
epifluorescence CPL microscope	Pal, Parker et al.	CPL*i*	CPM	chiral lanthanide(III) complexes onto paper substrate and incorporated in living cells	[94],[95]
CPL-LSCM	Pal, Parker et al.	CPL*i*	CPM	chiral lanthanide(III) complexes onto glass substrate and incorporated in living cells	[96]
VCD microsampling	Nafie et al.	VCD*i*	LCS	insulin fibrils and a lysozyme thin film	[97]
custom-built QCL-equipped microscope	Bhargava et al.	VCD*i*	CPM	biological tissue samples (colon tissue cores) with various grades of malignant	[98]
QCL-VCD	Sato, Koshoubu et al.	VCD*i*	CPM	KBr pellets containing α-amino acids; biological samples	[99],[100],[101]

tioned experimental set-ups for spatially resolved chiroptical spectroscopies.

The application of spatially resolved chiroptical spectroscopies has opened the way to new possibilities in the characterization of thin film of organic π-conjugated dyes: apparently homogeneous samples often revealed local heterogeneities and polymorphism, due to concomitant aggregation pathways associated with different chiroptical features. These techniques are very helpful for clarifying structure-property relationships of thin films, and therefore for adjusting all the parameters to

obtain reproducible samples with optimal performance as active layers in optoelectronic devices. We foresee that chiroptical imaging will find new subjects while embodying new instrumental configurations.

Acknowledgements

Conflict of Interests

The authors declare no conflict of interest.

Data Availability Statement

Data sharing is not applicable to this article as no new data were created or analyzed in this study.

[1] a) A. Facchetti, *Chem. Mater.* **2011**, *23*, 733–758; b) G. M. Farinola, R. Ragni, *Chem. Soc. Rev.* **2011**, *40*, 3467–3482; c) C. Wang, H. Dong, W. Hu, Y. Liu, D. Zhu, *Chem. Rev.* **2012**, *112*, 2208–2267.

[2] Y. Zhang, L. Guo, X. Zhu, X. Sun, *Front. Chem.* **2020**, *8*.

[3] a) G. P. Neupane, W. Ma, T. Yildirim, Y. Tang, L. Zhang, Y. Lu, *Nano Materials Science* **2019**, *1*, 246–259; b) J. Qi, Z. Chen, P. Jiang, W. Hu, Y. Wang, Z. Zhao, X. Cao, S. Zhang, R. Tao, Y. Li, D. Fang, *Adv. Sci.* **2022**, *9*, 2102662.

[4] a) Y. S. Rim, S.-H. Bae, H. Chen, N. De Marco, Y. Yang, *Adv. Mater.* **2016**, *28*, 4415–4440; b) R.-P. Xu, Y.-Q. Li, J.-X. Tang, *J. Mater. Chem. C* **2016**, *4*, 9116–9142.

[5] a) F. J. M. Hoeben, P. Jonkheijm, E. W. Meijer, A. P. H. J. Schenning, *Chem. Rev.* **2005**, *105*, 1491–1546; b) J. Deng, L. Zheng, C. Ding, Y. Guo, Y. Xie, J. Wang, Y. Ke, M. Li, L. Li, R. A. J. Janssen, *Adv. Funct. Mater.* **2023**, *33*, 2209195.

[6] a) V. Palermo, P. Samorì, *Angew. Chem. Int. Ed.* **2007**, *46*, 4428–4432; b) A. Salleo, R. J. Kline, D. M. DeLongchamp, M. L. Chabinyc, *Adv. Mater.* **2010**, *22*, 3812–3838; c) J. Rivnay, S. C. B. Mannsfeld, C. E. Miller, A. Salleo, M. F. Toney, *Chem. Rev.* **2012**, *112*, 5488–5519.

[7] a) J. Gierschner, J. Cornil, H.-J. Egelhaaf, *Adv. Mater.* **2007**, *19*, 173–191; b) J. Roncali, *Macromol. Rapid Commun.* **2007**, *28*, 1761–1775; c) O. Ostroverkhova, *Chem. Rev.* **2016**, *116*, 13279–13412.

[8] a) Y. Diao, L. Shaw, Z. Bao, S. C. B. Mannsfeld, *Energy Environ. Sci.* **2014**, *7*, 2145–2159; b) A. M. Hiszpanski, R. M. Baur, B. Kim, N. J. Tremblay, C. Nuckolls, A. R. Woll, Y.-L. Loo, *J. Am. Chem. Soc.* **2014**, *136*, 15749–15756; c) M. Chang, G. T. Lim, B. Park, E. Reichmanis, *Polymer* **2017**, *9*, 212.

[9] a) P. A. Korevaar, T. F. A. de Greef, E. W. Meijer, *Chem. Mater.* **2014**, *26*, 576–586; b) Y. Dorca, E. E. Greciano, J. S. Valera, R. Gómez, L. Sánchez, *Chem. Eur. J.* **2019**, *25*, 5848–5864.

[10] a) T. L. Andrew, T. M. Swager, *J. Polym. Sci. Part B* **2011**, *49*, 476–498; b) M. Verswyvel, G. Koeckelberghs, *Polym. Chem.* **2012**, *3*, 3203–3216; c) M. Liu, L. Zhang, T. Wang, *Chem. Rev.* **2015**, *115*, 7304–7397.

[11] a) C. Resta, S. Di Pietro, M. Majerić Elenkov, Z. Hameršak, G. Pescitelli, L. Di Bari, *Macromolecules* **2014**, *47*, 4847–4850; b) O. Hassan Omar, M. Falcone, A. Operamolla, G. Albano, *New J. Chem.* **2021**, *45*, 12016–12023.

[12] a) C. C. Lee, C. Grenier, E. W. Meijer, A. P. H. J. Schenning, *Chem. Soc. Rev.* **2009**, *38*, 671–683; b) Y. Yang, Y. Zhang, Z. Wei, *Adv. Mater.* **2013**, *25*, 6039–6049.

[13] C. Zhang, Y. Yan, Y. S. Zhao, J. Yao, *Acc. Chem. Res.* **2014**, *47*, 3448–3458.

[14] a) M. Hu, H.-T. Feng, Y.-X. Yuan, Y.-S. Zheng, B. Z. Tang, *Coord. Chem. Rev.* **2020**, *416*, 213329; b) A. Nitti, D. Pasini, *Adv. Mater.* **2020**, *32*, 1908021; c) F. Song, Z. Zhao, Z. Liu, J. W. Y. Lam, B. Z. Tang, *J. Mater. Chem. C* **2020**, *8*, 3284–3301; d) C. Liu, J.-C. Yang, J. W. Y. Lam, H.-T. Feng, B. Z. Tang, *Chem. Sci.* **2022**, *13*, 611–632.

[15] a) Y. Yang, R. C. da Costa, M. J. Fuchter, A. J. Campbell, *Nat. Photonics* **2013**, *7*, 634–638; b) L. Zhang, I. Song, J. Ahn, M. Han, M. Linares, M. Surin, H.-J. Zhang, J. H. Oh, J. Lin, *Nat. Commun.* **2021**, *12*, 142; c) X. Shang, L. Wan, L. Wang, F. Gao, H. Li, *J. Mater. Chem. C* **2022**, *10*, 2400–2410.

[16] a) G. Albano, L. A. Aronica, A. Minotto, F. Cacialli, L. Di Bari, *Chem. Eur. J.* **2020**, *26*, 16622–16627; b) D.-W. Zhang, M. Li, C.-F. Chen, *Chem. Soc. Rev.* **2020**, *49*, 1331–1343; c) K. Dhbaibi, L. Abella, S. Meunier-Della-Gatta, T. Roisnel, N. Vanthuyne, B. Jamoussi, G. Pieters, B. Racine, E. Quesnel, J. Autschbach, J. Crassous, L. Favereau, *Chem. Sci.* **2021**, *12*, 5522–5533.

[17] L. Torsi, G. M. Farinola, F. Marinelli, M. C. Tanese, O. H. Omar, L. Valli, F. Babudri, F. Palmisano, P. G. Zambonin, F. Naso, *Nat. Mater.* **2008**, *7*, 412–417.

[18] a) L. Dong, Y. Zhang, X. Duan, X. Zhu, H. Sun, J. Xu, *Anal. Chem.* **2017**, *89*, 9695–9702; b) J. G. Ibanez, M. E. Rincón, S. Gutierrez-Granados, M. H. Chahma, O. A. Jaramillo-Quintero, B. A. Frontana-Uribe, *Chem. Rev.* **2018**, *118*, 4731–4816.

[19] a) C. Train, M. Gruselle, M. Verdaguer, *Chem. Soc. Rev.* **2011**, *40*, 3297–3312; b) F. Pop, N. Zigon, N. Avarvari, *Chem. Rev.* **2019**, *119*, 8435–8478; c) G. L. J. A. Rikken, N. Avarvari, *Nat. Commun.* **2022**, *13*, 3564.

[20] a) P. C. Mondal, C. Fontanesi, D. H. Waldeck, R. Naaman, *Acc. Chem. Res.* **2016**, *49*, 2560–2568; b) R. Naaman, Y. Paltiel, D. H. Waldeck, *Nat. Chem. Rev.* **2019**, *3*, 250–260; c) F. Evers, A. Aharony, N. Bar-Gill, O. Entin-Wohlman, P. Hedegård, O. Hod, P. Jelinek, G. Kamieniarz, M. Lemeshko, K. Michaeli, V. Mujica, R. Naaman, Y. Paltiel, S. Refaely-Abramson, O. Tal, J. Thijssen, M. Thoss, J. M. van Ruitenbeek, L. Venkataraman, D. H. Waldeck, B. Yan, L. Kronik, *Adv. Mater.* **2022**, *34*, 2106629.

[21] a) C. Wang, H. Fei, Y. Qiu, Y. Yang, Z. Wei, Y. Tian, Y. Chen, Y. Zhao, *Appl. Phys. Lett.* **1999**, *74*, 19–21; b) J. R. Brandt, F. Salerno, M. J. Fuchter, *Nat. Chem. Rev.* **2017**, *1*, 0045; c) Y. He, S. Lin, J. Guo, Q. Li, *Aggregate* **2021**, *2*, e141.

[22] a) Y. Olivier, D. Niedzialek, V. Lemaur, W. Pisula, K. Müllen, U. Koldemir, J. R. Reynolds, R. Lazzaroni, J. Cornil, D. Beljonne, *Adv. Mater.* **2014**, *26*, 2119–2136; b) M. Mladenović, N. Vukmirović, *Adv. Funct. Mater.* **2015**, *25*, 1915–1932; c) H. K. Bisoyi, Q. Li, *Angew. Chem. Int. Ed.* **2016**, *55*, 2994–3010; d) H. K. Bisoyi, Q. Li, *Chem. Rev.* **2022**, *122*, 4887–4926.

[23] a) F. J. Giessibl, *Rev. Mod. Phys.* **2003**, *75*, 949–983; b) J. CAZAUX, *J. Microsc.* **2005**, *217*, 16–35; c) Y. Lin, M. Zhou, X. Tai, H. Li, X. Han, J. Yu, *Matter* **2021**, *4*, 2309–2339.

[24] M. J. Booth, *Light-Sci. Appl.* **2014**, *3*, e165-e165.

[25] a) N. Berova, L. D. Bari, G. Pescitelli, *Chem. Soc. Rev.* **2007**, *36*, 914–931; b) G. Pescitelli, L. Di Bari, N. Berova, *Chem. Soc. Rev.* **2011**, *40*, 4603–4625; c) G. Pescitelli, L. Di Bari, N. Berova, *Chem. Soc. Rev.* **2014**, *43*, 5211–5233; d) G. Pescitelli, *Chirality* **2022**, *34*, 333–363.

[26] a) F. S. Richardson, J. P. Riehl, *Chem. Rev.* **1977**, *77*, 773–792; b) J. P. Riehl, F. S. Richardson, *Chem. Rev.* **1986**, *86*, 1–16; c) G. Longhi, E. Castiglioni, J. Koshoubu, G. Mazzeo, S. Abbate, *Chirality* **2016**, *28*, 696–707.

[27] G. Albano, G. Pescitelli, L. Di Bari, *Chem. Rev.* **2020**, *120*, 10145–10243.

[28] G. Albano, G. Pescitelli, L. Di Bari, *ChemNanoMat* **2022**, *8*, e202200219.

[29] a) A. Thomas, A. Chervy, S. Azzini, M. Li, J. George, C. Genet, T. W. Ebbesen, *J. Phys. Chem. C* **2018**, *122*, 14205–14212; b) O. Arteaga, B. Kahr, *J. Opt. Soc. Am. B* **2019**, *36*, F72-F83.

[30] a) O. Arteaga, Z. El-Hachemi, A. Canillas, J. M. Ribó, *Thin Solid Films* **2011**, *519*, 2617–2623; b) J. N. Hilfiker, H. Nong, S. Schoeche, *Adv. Opt. Technol.* **2022**, *11*, 59–91.

[31] M. F. Maestre, J. E. Katz, *Biopolymers* **1982**, *21*, 1899–1908.

[32] M. F. Maestre, G. Salzman, R. Tobey, C. Bustamante, *Biochemistry* **1985**, *24*, 5152–5157.

[33] F. Livolant, M. F. Maestre, *Biochemistry* **1988**, *27*, 3056–3068.

[34] F. Livolant, W. Mickols, M. F. Maestre, *Biopolymers* **1988**, *27*, 1761–1769.

[35] Y. Shindo, M. Nishio, S. Maeda, *Biopolymers* **1990**, *30*, 405–413.

[36] a) H. P. Jensen, J. A. Schellman, T. Troxell, *Appl. Spectrosc.* **1978**, *32*, 192–200; b) A. Schönhofer, H.-G. Kuball, C. Puebla, *Chem. Phys.* **1983**, *76*, 453–467; c) J. Schellman, H. P. Jensen, *Chem. Rev.* **1987**, *87*, 1359–1399.

[37] K. Claborn, E. Puklin-Faucher, M. Kurimoto, W. Kaminsky, B. Kahr, *J. Am. Chem. Soc.* **2003**, *125*, 14825–14831.

[38] K. Claborn, A.-S. Chu, S.-H. Jang, F. Su, W. Kaminsky, B. Kahr, *Cryst. Growth Des.* **2005**, *5*, 2117–2123.

[39] E. Gunn, R. Sours, J. B. Benedict, B. Kahr, *J. Am. Chem. Soc.* **2006**, *128*, 14234–14235.

[40] J. H. Freudenthal, E. Hollis, B. Kahr, *Chirality* **2009**, *21*, E20-E27.

[41] A. Matsugaki, H. Takechi, H. Monjushiro, H. Watarai, *Anal. Sci.* **2008**, *24*, 297–300.

[42] M. Savoini, X. Wu, M. Celebrano, J. Ziegler, P. Biagioni, S. C. J. Meskers, L. Duò, B. Hecht, M. Finazzi, *J. Am. Chem. Soc.* **2012**, *134*, 5832–5835.

[43] G. Lakhwani, J. Gielen, M. Kemerink, P. C. M. Christianen, R. A. J. Janssen, S. C. J. Meskers, *J. Phys. Chem. B* **2009**, *113*, 14047–14051.

[44] M. Oda, H. G. Nothofer, G. Lieser, U. Scherf, S. C. J. Meskers, D. Neher, *Adv. Mater.* **2000**, *12*, 362–365.

[45] T. Narushima, H. Okamoto, *Phys. Chem. Chem. Phys.* **2013**, *15*, 13805–13809.

[46] T. Narushima, H. Okamoto, *J. Phys. Chem. C* **2013**, *117*, 23964–23969.

[47] F. Tantussi, F. Fuso, M. Allegrini, N. Micali, I. G. Occhiuto, L. M. Scolaro, S. Patanè, *Nanoscale* **2014**, *6*, 10874–10878.

[48] T. Narushima, H. Okamoto, *Sci. Rep.* **2016**, *6*, 35731.

[49] T. Yamada, T. Eguchi, T. Wakiyama, T. Narushima, H. Okamoto, N. Kimizuka, *Chem. Eur. J.* **2019**, *25*, 6698–6702.

[50] P. Szustakiewicz, N. Kowalska, D. Grzelak, T. Narushima, M. Góra, M. Bagiński, D. Pociecha, H. Okamoto, L. M. Liz-Marzán, W. Lewandowski, *ACS Nano* **2020**, *14*, 12918–12928.

[51] R. Nakajima, D. Hirobe, G. Kawaguchi, Y. Nabei, T. Sato, T. Narushima, H. Okamoto, H. M. Yamamoto, *Nature* **2023**, *613*, 479–484.

[52] C. Roche, H.-J. Sun, P. Leowanawat, F. Araoka, B. E. Partridge, M. Peterca, D. A. Wilson, M. E. Prendergast, P. A. Heiney, R. Graf, H. W. Spiess, X. Zeng, G. Ungar, V. Percec, *Nat. Chem.* **2016**, *8*, 80–89.

[53] L. Wang, B. E. Partridge, N. Huang, J. T. Olsen, D. Sahoo, X. Zeng, G. Ungar, R. Graf, H. W. Spiess, V. Percec, *J. Am. Chem. Soc.* **2020**, *142*, 9525–9536.

[54] J.-J. Lee, B.-C. Kim, H.-J. Choi, S. Bae, F. Araoka, S.-W. Choi, *ACS Nano* **2020**, *14*, 5243–5250.

[55] H. Satozono, *Japanese Patent*, P5537310, 2014–07-02, **2014**.

[56] Y. Kushida, T. Sawato, N. Saito, M. Shigeno, H. Satozono, M. Yamaguchi, *ChemPhysChem* **2016**, *17*, 3283–3288.

[57] S. C. Karunakaran, B. J. Cafferty, A. Weigert-Muñoz, G. B. Schuster, N. V. Hud, *Angew. Chem. Int. Ed.* **2019**, *58*, 1453–1457.

[58] M. Morgenroth, M. Scholz, M. J. Cho, D. H. Choi, K. Oum, T. Lenzer, *Nat. Commun.* **2022**, *13*, 210.

[59] R. Abbel, A. P. H. J. Schenning, E. W. Meijer, *Macromolecules* **2008**, *41*, 7497–7504.

[60] M. Morgenroth, M. Scholz, L. Guy, K. Oum, T. Lenzer, *Angew. Chem. Int. Ed.* **2022**, *61*, e202203075.

[61] a) T. Jávorfi, R. Hussain, D. Myatt, G. Siligardi, *Chirality* **2010**, *22*, E149-E153; b) R. Hussain, T. Javorfi, G. Siligardi, *J. Synchrotron Radiat.* **2012**, *19*, 132–135; c) R. Hussain, K. Benning, T. Javorfi, E. Longo, T. R. Rudd, B. Pulford, G. Siligardi, *J. Synchrotron Radiat.* **2015**, *22*, 465–468.

[62] R. Hussain, T. Jávorfi, G. Siligardi, *Front. Chem.* **2021**, *9*.

[63] F. Zinna, C. Resta, M. Górecki, G. Pescitelli, L. Di Bari, T. Jávorfi, R. Hussain, G. Siligardi, *Macromolecules* **2017**, *50*, 2054–2060.

[64] G. Albano, F. Salerno, L. Portus, W. Porzio, L. A. Aronica, L. Di Bari, *ChemNanoMat* **2018**, *4*, 1059–1070.

[65] G. Albano, M. Górecki, G. Pescitelli, L. Di Bari, T. Javorfi, R. Hussain, G. Siligardi, *New J. Chem.* **2019**, *43*, 14584–14593.

[66] G. Albano, M. Lissia, G. Pescitelli, L. A. Aronica, L. Di Bari, *Mater. Chem. Front.* **2017**, *1*, 2047–2056.

[67] G. Albano, M. Górecki, T. Jávorfi, R. Hussain, G. Siligardi, G. Pescitelli, L. Di Bari, *Aggregate* **2022**, *3*, e193.

[68] M. Górecki, F. Lipparini, G. Albano, T. Jávorfi, R. Hussain, G. Siligardi, G. Pescitelli, L. Di Bari, *Chem. Eur. J.* **2022**, *28*, e202103632.

[69] J. Wade, J. N. Hilfiker, J. R. Brandt, L. Liirò-Peluso, L. Wan, X. Shi, F. Salerno, S. T. J. Ryan, S. Schöche, O. Arteaga, T. Jávorfi, G. Siligardi, C. Wang, D. B. Amabilino, P. H. Beton, A. J. Campbell, M. J. Fuchter, *Nat. Commun.* **2020**, *11*, 6137.

[70] D.-M. Răsădean, T.-M. Gianga, T. Jávorfi, R. Hussain, G. Siligardi, G. D. Pantoş, *Molecules* **2020**, *25*.

[71] J. Humphreys, C. E. Killalea, F. Pop, E. S. Davies, G. Siligardi, D. B. Amabilino, *Chirality* **2023**, *35*, 281–297.

[72] R. Hussain, T. Jávorfi, C. S. Hughes, H. Sriram, R. Lashminarayanan, G. Siligardi, *Symmetry* **2020**, *12*, 1847.

[73] A. Taddeucci, F. Zinna, G. Siligardi, L. Di Bari, *Chem. Biomed. Imaging* **2023**, DOI: 10.1021/cbmi.1023c00049.

[74] F. Zinna, G. Albano, A. Taddeucci, T. Colli, L. A. Aronica, G. Pescitelli, L. Di Bari, *Adv. Mater.* **2020**, *32*, 2002575.

[75] A. Le Gratiet, A. Mohebi, F. Callegari, P. Bianchini, A. Diaspro, *Appl. Sci.* **2021**, *11*, 1632.

[76] J. M. Bueno, P. Artal, *Opt. Lett.* **1999**, *24*, 64–66.

[77] a) D. Lara, C. Dainty, *Appl. Opt.* **2006**, *45*, 1917–1930; b) R. M. A. Azzam, *Opt. Lett.* **1985**, *10*, 309–311.

[78] K. M. Twietmeyer, R. A. Chipman, A. E. Elsner, Y. Zhao, D. VanNasdale, *Opt. Express* **2008**, *16*, 21339–21354.

[79] N. Mazumder, L. Y. Xiang, J. Qiu, F.-J. Kao, *Sci. Rep.* **2017**, *7*, 45816.

[80] I. Saytashev, S. Saha, J. Chue-Sang, P. Lopez, M. Laughrey, J. C. Ramella-Roman, *Opt. Lett.* **2020**, *45*, 2168–2171.

[81] O. Arteaga, J. Freudenthal, B. Wang, B. Kahr, *Appl. Opt.* **2012**, *51*, 6805–6817.

[82] O. Arteaga, M. Baldrís, J. Antó, A. Canillas, E. Pascual, E. Bertran, *Appl. Opt.* **2014**, *53*, 2236–2245.

[83] D. Gottlieb, O. Arteaga, *Opt. Express* **2021**, *29*, 34723–34734.

[84] C. E. Killalea, M. Samperi, G. Siligardi, D. B. Amabilino, *Chem. Commun.* **2022**, *58*, 4468–4471.

[85] S. R. Clowes, D. M. Răsădean, T.-M. Gianga, T. Jávorfi, R. Hussain, G. Siligardi, G. D. Pantoş, *Molecules* **2023**, *28*, 1523.

[86] I. Favorskiy, D. Vu, E. Peytavit, S. Arscott, D. Paget, A. C. H. Rowe, *Rev. Sci. Instrum.* **2010**, *81*, 103902.

[87] H. Tsumatori, T. Harada, J. Yuasa, Y. Hasegawa, T. Kawai, *Appl. Phys. Express* **2011**, *4*, 011601.

[88] J. Kumar, T. Nakashima, H. Tsumatori, M. Mori, M. Naito, T. Kawai, *Chem. Eur. J.* **2013**, *19*, 14090–14097.

[89] Y. Imai, Y. Nakano, T. Kawai, J. Yuasa, *Angew. Chem. Int. Ed.* **2018**, *57*, 8973–8978.

[90] K. Katayama, S. Hirata, M. Vacha, *Phys. Chem. Chem. Phys.* **2014**, *16*, 17983–17987.

[91] D. Di Nuzzo, C. Kulkarni, B. Zhao, E. Smolinsky, F. Tassinari, S. C. J. Meskers, R. Naaman, E. W. Meijer, R. H. Friend, *ACS Nano* **2017**, *11*, 12713–12722.

[92] A. Sharma, A. Campbell, J. Leoni, Y. T. Cheng, M. Müllner, G. Lakhwani, *J. Phys. Chem. Lett.* **2019**, *10*, 7547–7553.

[93] H. Koike, K. Nozaki, M. Iwamura, *Chem. Asian J.* **2020**, *15*, 85–90.

[94] A. T. Frawley, R. Pal, D. Parker, *Chem. Commun.* **2016**, *52*, 13349–13352.

[95] A. T. Frawley, H. V. Linford, M. Starck, R. Pal, D. Parker, *Chem. Sci.* **2018**, *9*, 1042–1049.

[96] P. Stachelek, L. MacKenzie, D. Parker, R. Pal, *Nat. Commun.* **2022**, *13*, 553.

[97] X. Lu, H. Li, J. W. Nafie, T. Pazderka, M. Pazderková, R. K. Dukor, L. A. Nafie, *Appl. Spectrosc.* **2017**, *71*, 1117–1126.

[98] Y. Phal, K. Yeh, R. Bhargava, *Anal. Chem.* **2021**, *93*, 1294–1303.

[99] H. Sato, M. Shimizu, K. Watanabe, J. Yoshida, I. Kawamura, J. Koshoubu, *Anal. Chem.* **2021**, *93*, 2742–2748.

[100] H. Sato, M. Shimizu, K. Watanabe, J. Yoshida, I. Kawamura, *Chem. Lett.* **2021**, *50*, 1543–1545.

[101] H. Sato, A. Yamagishi, M. Shimizu, K. Watanabe, J. Koshoubu, J. Yoshida, I. Kawamura, *J. Phys. Chem. Lett.* **2021**, *12*, 7733–7737.

[102] M. A. J. Koenis, A. Osypenko, G. Fuks, N. Giuseppone, V. P. Nicu, L. Visscher, W. J. Buma, *J. Am. Chem. Soc.* **2020**, *142*, 1020–1028.
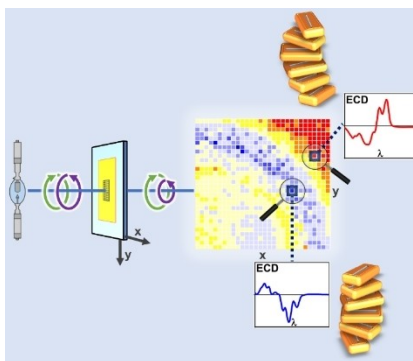
REVIEW

A critical and up-to-date overview is given on spatially resolved chiroptical spectroscopies, which represent a promising tool for mapping and disentangling local supramolecular structures in thin films of chiral organic dyes.

Dr. G. Albano, A. Taddeucci, Prof. G. Pescitelli, Prof. L. Di Bari*, Selected by the Editorial Office for our Showcase of outstanding Review-type articles .

1 – 24

Spatially Resolved Chiroptical Spectroscopies Emphasizing Recent Applications to Thin Films of Chiral Organic Dyes